AGU PUBLICATIONS

JGR

Journal of Geophysical Research: Earth Surface

RESEARCH ARTICLE
10.1002/2016JF003839

Key Points:
- The current Barnes Ice cap geometry cannot be stable
- The stability of the ice cap is affected by surge zone and basal Pleistocene ice layer
- The mean 1960-2013 climate was the limit for sustainable climatic condition

Supporting Information:
- Supporting Information S1

Correspondence to:
A. Gilbert,
adrieng@sfu.ca

Citation:
Gilbert, A., G. E. Flowers, G. H. Miller, B. T. Rabus, W. Van Wychen, A. S. Gardner, and L. Copland (2016), Sensitivity of Barnes Ice Cap, Baffin Island, Canada, to climate state and internal dynamics, *J. Geophys. Res. Earth Surf.*, *121*, 1516–1539, doi:10.1002/2016JF003839.

Received 29 JAN 2016
Accepted 26 JUL 2016
Accepted article online 29 JUL 2016
Published online 26 AUG 2016

Sensitivity of Barnes Ice Cap, Baffin Island, Canada, to climate state and internal dynamics

A. Gilbert[1], G. E. Flowers[1], G. H. Miller[2], B. T. Rabus[1], W. Van Wychen[3], A. S. Gardner[4], and L. Copland[3]

[1]Department of Earth Sciences, Simon Fraser University, Burnaby, British Columbia, Canada, [2]INSTAAR and Department of Geological Sciences, University of Colorado Boulder, Boulder, Colorado, USA, [3]Department of Geography, Environment and Geomatics, University of Ottawa, Ottawa, Ontario, Canada, [4]Jet Propulsion Laboratory, California Institute of Technology, Pasadena, California, USA

Abstract Barnes Ice Cap is a remnant of the Laurentide Ice Sheet, which covered much of northern North America during the Last Glacial Maximum. Barnes reached a quasi-equilibrium state ~2000 years ago and has remained similar in size since then, with a small increase during the Little Ice Age. In this study, we combine historical observations (1960–1980) with more recent satellite and airborne data (1995–2010) to drive a mass balance model coupled to a transient thermomechanical model with an adaptive mesh geometry. The model is used to characterize the current state of the ice cap and to investigate its stability as a function of climate and its own internal dynamics. On millennial time scales we show that ice flow is influenced by adjustment of an unsteady shape, by gently sloping bedrock, and by contrasting viscosities between the Pleistocene and Holocene ice. On shorter time scales, Barnes is affected by surge activity. Sensitivity tests reveal that Barnes experienced climate conditions which enabled its stability 2000 to 3000 years ago but will disappear under current climate conditions in the next millennium.

1. Introduction

The Canadian Arctic Archipelago is covered by ~146,000 km^2 of glacier ice and contains one third of the global volume of land ice outside the Antarctic and Greenland ice sheets [*Radić and Hock*, 2010]. These ice masses were significant contributors to the sea level rise of the early 21st century, in response to increases in summer air temperature in the region [*Gardner et al.*, 2011, 2012]. Both ice caps and valley glaciers in this region are known to be generally polythermal [*Blatter*, 1987; *Copland and Sharp*, 2001], characterized by a core of temperate basal ice in the central ablation zone ("Canadian-type" thermal structure) [*Blatter and Hutter*, 1991]. Such thermal structure leads to complex dynamics [*Bingham et al.*, 2006] where the hydrological system is strongly influenced by ice temperature. More than 50 glaciers have been identified as surge type in the northern Archipelago [*Copland et al.*, 2003], and in the southern Archipelago, 10 surge-type glaciers have been described on Bylot Island [*Dowdeswell et al.*, 2007] and five surge areas on Barnes Ice Cap [*Holdsworth*, 1977].

Previous studies have indicated that an equilibrium line altitude above 650 m is required for Barnes Ice Cap to maintain a steady state [*Mahaffy*, 1976; *Hooke et al.*, 1987], meaning that Barnes is situated on sufficiently low and flat bedrock that ice cap inception under present-day conditions would be impossible. This peculiarity arises from the fact that Barnes is a remnant of the Laurentide Ice Sheet, which covered much of northern North America during the Last Glacial Maximum around 21 ka B.P. [*Briner et al.*, 2009; *Dyke et al.*, 2003; *Hooke*, 1976]. The Laurentide retreated (Figure 1) over the Holocene to the current margin of Barnes Ice Cap by ~2 ka B.P. [*Briner et al.*, 2009] and has remained in quasi-equilibrium with climate since then. The existence of an accumulation zone is due only to the height of the ice cap itself, making Barnes a "self-sustaining" ice mass particularly sensitive to both climate and internal dynamics. The local surge activity of Barnes [*Holdsworth*, 1977] affects the shape of the ice cap with the presence of several lobate structures on its westside, making Barnes asymmetric along its longitudinal axis [*Mahaffy*, 1976]. Under certain atmospheric conditions, a change in the geometry of the ice cap resulting from modified ice flow could cause it to cross a threshold that would lead to its eventual demise.

To investigate the sensitivity of Barnes to climate and internal dynamics, the Stokes equations were solved using a thermomechanical finite element model based on the Elmer/Ice code [*Gagliardini et al.*, 2013] in which we introduce an adaptive mesh, which allows the ice cap edge to move. Basal sliding is inferred using a control inverse method [*MacAyeal*, 1992; *Gillet-Chaulet et al.*, 2012], where we minimize a cost function

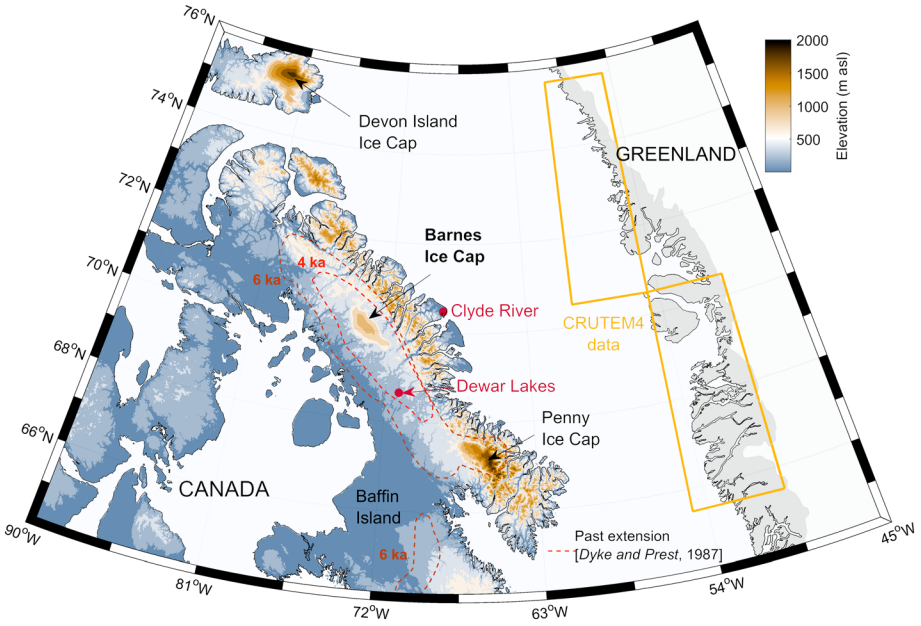

Figure 1. Location of Baffin Island, of Barnes Ice Cap, and of meteorological stations used in this study (Dewar Lakes and Clyde River). Dashed lines indicate the past ice extent as reconstructed by *Dyke and Prest* [1987]. Color scale is the surface elevation (except for Greenland).

calculated from the combination of the measured rate of surface elevation change and surface velocities. The ice flow model is coupled to a mass balance model and includes a basal layer of Pleistocene ice with a distinct viscosity [*Hooke*, 1976]. The main objectives of this study are to better understand the history of Barnes ice cap and to establish a model that can be used to predict the response of the ice cap to future climate change.

2. Study Site

2.1. Context

Barnes Ice Cap (latitude 70°N, longitude 73°W) is located in the center of Baffin Island, Canada (Figure 1), covers an area of ~5800 km^2 [*Gardner et al.*, 2012], and has a total mass of ~2000 Gt (estimated in this study). The ice cap is approximately 150 km long and 60 km wide and is characterized by three main domes (Figure 2). Maximum ice thickness of ~730 m is found in a bedrock depression between the north and central domes, although the maximum ice elevation of 1124 m above sea level (asl) occurs at the summit of the north dome. The dynamics of Barnes is influenced by fast flow anomalies that have been linked to surge activity and are responsible for the formation of visible lobes along the west and south margins of the ice cap (Figure 2) [*Holdsworth*, 1977] and by calving in Bieler and Conn lakes on the north side (Figure 2). After a period of quasi-equilibrium with climate over the past two millennia, Barnes is now losing mass at a high rate of 2.8 Gt yr^{-1} (1960–2010 period) [*Gardner et al.*, 2012] and appears to have accumulated mass only by superimposed ice formation in most recent years [*Dupont*, 2013]. This change is likely associated with increasing summer air temperatures in the region [*Sneed et al.*, 2008; *Hooke et al.*, 1987; *Gardner et al.*, 2012; *Lenaerts et al.*, 2013; *Sharp et al.*, 2011].

2.2. Data

Barnes is the most studied ice mass on Baffin Island, with a mass balance measurement program established in the 1960s [*Sagar*, 1966; *Loken and Sagar*, 1967]. In the 1970s and 1980s, research focused primarily on the south dome with measurements of mass balance [*Hooke et al.*, 1987; *Holdsworth and Hooke*, 1977], borehole temperature [*Hooke et al.*, 1980; *Classen*, 1977], ice deformation [*Hooke and Hanson*, 1986] (see location on Figure 2), surface velocities [*Hooke et al.*, 1987], and isotopic composition of the ice [*Hooke and Clausen*, 1982]. The 1990s marked the end of most in situ studies and the onset of satellite or airborne measurements providing detailed measurements of margin displacements [*Jacobs et al.*, 1993, 1997], elevation changes

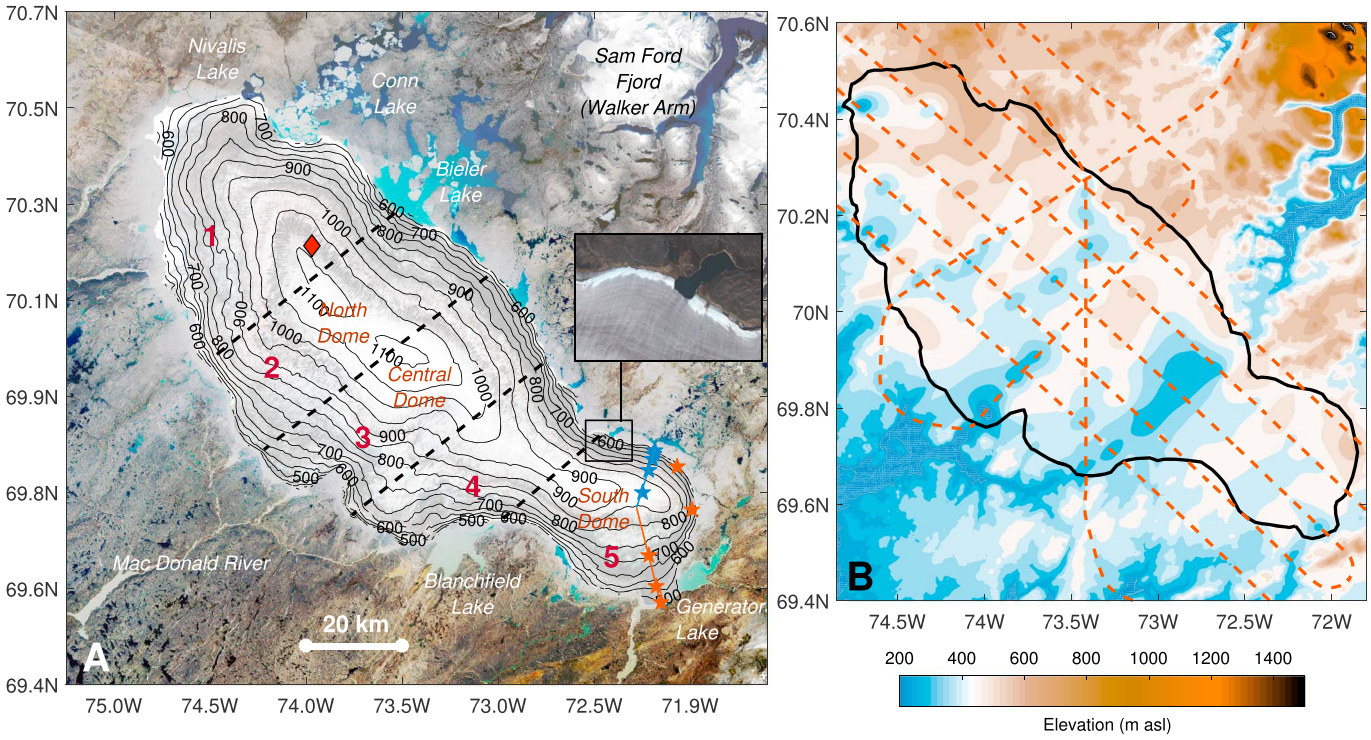

Figure 2. Barnes Ice Cap surface and bed topography. (a) Map of Barnes Ice Cap (Landsat 5 image, 9 August 2010, with contour lines from the Canadian Digital Elevation Data, 1960). The five zones delimited by black dashed lines are those used by *Loken and Sagar* [1967] for mass balance estimation. Red diamond shows the location of the 1962–1963 field camp [*Sagar*, 1966]. Blue stars show the locations of borehole temperature and ice deformation measurements [*Hooke et al*., 1980; *Hooke and Hanson*, 1986]; red stars mark borehole temperature measurements only [*Hooke et al*., 1980; *Classen*, 1977]. Blue line shows the location of the velocity and mass balance profile measurements of *Hooke et al*. [1987]. Red line marks the velocity profile from *Loken et al*. [1968]. (b) The 2011 NASA IceBridge airborne radar measurement tracks (orange dashed lines) and interpolated bedrock topography. Black line is the Barnes Ice Cap outline in 2010 from the Landsat 5 image.

[*Gray et al*., 2015; *Gardner et al*., 2012; *Abdalati et al*., 2004], surface velocities [*Van Wychen et al*., 2015], and surface melt duration [*Dupont et al*., 2012]. In this study we also derive a new data set of one-dimensional surface velocity observations using interferometric synthetic aperture radar (InSAR) analysis on a pair of ERS InSAR scenes from European Remote-sensing Satellites (ERS) from 31 March 1996 to 1 April 1996. In 2011 NASA's Operation IceBridge obtained ice thickness measurements from airborne radar (Figure 2), which allows us to model Barnes with a realistic bed topography.

We make use of four different sources of climate data for mass balance modeling: (i) meteorological station data at Clyde River (Baffin Bay coast, about 200 km east of Barnes, see Figure 1), (ii) meteorological station data at Dewar Lakes (inland, about 200 km south of Barnes; see Figure 1), (iii) gridded temperature and precipitation data statistically interpolated by *Hutchinson et al*. [2009], and (iv) the CRUTEM4 data set which is a gridded data set of global historical near-surface air temperature anomalies over land on a 5° grid [*Jones et al*., 2012]. Data sources i, ii, and iii begin in 1960. For the fourth, we use the nearest valid cells for 1870 to present. The corresponding grid cells are located 800 km east of Barnes on the Greenland coast at the same mean latitude (see Figure 1). The annual mean temperature correlation between the averaged CRUTEM4 data and Dewar Lakes or Clyde River is $R^2 = 0.7$ ($n = 52$).

3. Modeling Methods

3.1. Thermomechanical Ice Flow Model

The ice flow model is based on the Stokes equations adopting Glen's flow law for viscous isotropic ice [*Cuffey and Paterson*, 2010] and coupled to an energy conservation equation using the enthalpy formulation [*Aschwanden et al*., 2012; *Gilbert et al*., 2014]. Changes in the ice cap surface elevation are computed by solving a free surface equation [*Gilbert et al*., 2014]. Details on the model and boundary conditions can be found in the supporting information.

3.2. Basal Pleistocene Ice Layer

Barnes is characterized by the presence of a Pleistocene ice layer (PIL) at the base of the ice cap [*Hooke*, 1976], visible as a white band along the ice margin (Figure 2a, inset). It has been demonstrated by borehole deformation measurements that this layer is appreciably softer than the Holocene ice above it [*Hooke and Hanson*, 1986]. A Pleistocene ice layer is included in the model as a body that forms an internal boundary, with a specified enhancement factor E distinct from Holocene ice. Evolution of the PIL thickness is permitted by solving a free surface-type equation at the interface between Pleistocene and Holocene ice:

$$\frac{\partial z_{\text{pil}}}{\partial t} + u_{\text{pil}}\frac{\partial z_{\text{pil}}}{\partial x} + v_{\text{pil}}\frac{\partial z_{\text{pil}}}{\partial y} - w_{\text{pil}} = 0, \tag{1}$$

where z_{pil} is the interface elevation (m) and (u_{pil}, v_{pil}, and w_{pil}) are the ice velocity components (m s^{-1}) at location (x, y, and z) on the interface. Our method of estimating the initial distribution of the PIL is described in section 4.2.1.2.

3.3. Surface Mass Balance Model

Surface melting is modeled using the degree-day method [*Braithwaite*, 1995]. Since refreezing processes have been shown to make an important contribution to the total accumulation of Barnes [*Hooke et al.*, 1986; *Dupont*, 2013], net annual surface mass balance is determined by

$$M(x,y) = A_{\text{snow}}(x,y) + R(x,y) - M_{\text{melt}}(x,y), \tag{2}$$

where M is the net surface mass balance (kg m^{-2} yr^{-1}), A_{snow} is the total surface accumulation (kg m^{-2} yr^{-1}), R is the rate of superimposed ice formation (kg m^{-2} yr^{-1}), and M_{melt} is the surface ablation (kg m^{-2} yr^{-1}).

To make the parameter estimation process simpler and faster for mass balance calculations, annual mass balance is directly computed from annual accumulation and annual melt using cumulative positive degree-days (PDDs) over the year. Surface accumulation observations made by *Loken and Sagar* [1967] over the whole ice cap reveal a strong accumulation gradient along the long axis of Barnes (about twice the accumulation in Zone 5 compared to Zone 1; see Figure 2). The measured surface accumulation lapse rate also appears to increase along this axis. Such a feature is not observed in the climate data, so we introduce a parameter that scales surface accumulation along the long axis of Barnes. Surface accumulation on Barnes is calculated as a function of elevation (z) and distance along the long axis of the ice cap (d) with the northwest extremity as the origin:

$$A_{\text{snow}} = \begin{cases} \left(P_{\text{ref}} + (z - zp_{\text{ref}})\dfrac{\mathrm{d}P}{\mathrm{d}z}\right)(1.0 + (d - d_0)f_p)r_{\text{snow}} & \text{if} \quad d \geq d_0 \\ P_{\text{ref}} + (z - zp_{\text{ref}})\dfrac{\mathrm{d}P}{\mathrm{d}z} & \text{if} \quad d < d_0 \end{cases}, \tag{3}$$

where P_{ref} is the precipitation rate at the northwest extremity of Barnes (kg m^{-2} yr^{-1}), $zp_{\text{ref}} = 400$ m asl is the elevation at this point, dP/dz is the precipitation lapse rate (kg m^{-2} yr^{-1} m^{-1}), f_p is the longitudinal precipitation factor (km^{-1}), which is the rate of increase in accumulation with distance along the axis of the ice cap, d_0 (km) is the position where precipitation begins to increase, and r_{snow} is the ratio of accumulation to total precipitation. The value of r_{snow} is determined from air temperature and the snow/rain threshold T_p (K).

Accumulation on Barnes occurs primarily as superimposed ice, and we assume that refreezing only occurs in newly accumulated snow at the end of the accumulation season. Thus we write

$$R = \min(M_{\text{melt}}, f_r\, A_{\text{snow}}) \tag{4}$$

with f_r the refreezing factor, which is the fraction of the accumulation A_{snow} that melts and refreezes. Assuming that water refreezes only in the current year's snow and cannot percolate through the ice layers of previous summers, the volumetric constraint on f_r (volume available for refreezing) is

$$f_r < \frac{\left(1 - \frac{\rho_s}{\rho_i}\right)\frac{\rho_w}{\rho_s}}{1 + \left(1 - \frac{\rho_s}{\rho_i}\right)\frac{\rho_w}{\rho_s}}, \tag{5}$$

where ρ_i, ρ_s, and ρ_w are, respectively, the density (kg m^{-3}) of ice, snow, and water. Measured snow density at the top of the ice cap is about 350 kg m^{-3} [*Dupont*, 2013] and gives $f_r < 0.6$.

In order to work at an annual time step, we develop a specific formulation for the degree-day factor as a function of mean surface type (ice or snow) during the year by taking into account initial snow cover, superimposed ice formation, and total melting. The spatial distribution of the degree-day factor is recomputed each year as a function of the degree-day factors for snow and ice. This procedure allows us to take into account the snow albedo feedback. Ablation is calculated using a degree-day model with the degree-day factor f_m (kg m^{-2} K^{-1} yr^{-1}):

$$M_{\text{melt}} = P_{\text{DD}}\ f_m \tag{6}$$

and the number of positive degree-days per year (P_{DD}) defined as a function of elevation (z) by

$$P_{\text{DD}} = \sum_{i=1}^{365} d_{P_{\text{DD}}}(i) \tag{7}$$

with

$$\mathrm{d}_{P_{\text{DD}}}(i) = \begin{cases} T_{\text{ref}}(i) + \mathrm{d}T/\mathrm{d}z(z - z_{\text{ref}}) & \text{if} \quad T_{\text{ref}}(i) + \mathrm{d}T/\mathrm{d}z(z - z_{\text{ref}}) > T_m \\ 0 & \text{if} \quad T_{\text{ref}}(i) + \mathrm{d}T/\mathrm{d}z(z - z_{\text{ref}}) \leq T_m \end{cases}, \tag{8}$$

where T_{ref} (K) is the mean of daily air temperatures at Dewar Lakes and Clyde River meteorological stations, $z_{\text{ref}} = 276$ m asl is the mean elevation of the two stations, dT/dz is the temperature lapse rate (K m^{-1}), and T_m is a threshold temperature (K) above which melting occurs.

For each model year, the degree-day factor is calculated at each grid point using the following method: we first compute the ratio $r_{s/m}$ between accumulated snow (snow precipitation minus snow lost by superimposed ice formation) and total melt assuming $f_m = f_{\text{snow}}$:

$$r_{s/m} = \frac{A_{\text{snow}} - R\left(1 + \frac{\rho_w}{(1-\rho_s/\rho_i)\rho_s}\right)}{P_{\text{DD}}\ \ f_{\text{snow}}}. \tag{9}$$

We then have

$$f_m = \begin{cases} f_{\text{snow}} & \textit{if} \quad r_{s/m} \geq 1 \\ f_{\text{ice}} - (f_{\text{ice}} - f_{\text{snow}}) \times r_{s/m} & \textit{if} \quad r_{s/m} < 1 \end{cases}, \tag{10}$$

where f_{snow} is the degree-day factor for snow and f_{ice} that for ice. The firn thickness h_{firn} used for computing surface temperature (equation (12) in the supporting information) is updated at each time step:

$$h_{\text{firn}}(t + \mathrm{d}t) = h_{\text{firn}}(t) + \left(A_{\text{snow}} - R\left(1 + \frac{\rho_w}{(1 - \rho_s/\rho_i)\rho_s}\right) - f_m P_{\text{DD}}\right)\mathrm{d}t - h_{\text{firn}}(t)\mathrm{d}_{\text{firn}}\mathrm{d}t, \tag{11}$$

where d_{firn} is a regularization parameter (kg m^{-2} yr^{-1}) under the assumption of a firn thickness proportional to the accumulation in a steady state regime.

3.4. Numerical Solution

The thermomechanical model is solved using the finite element code Elmer/Ice [e.g., *Gagliardini et al.*, 2013] based on the Elmer open-source multiphysics package (see http://elmerice.elmerfem.org for details). To capture the evolution of ice cap geometry in prognostic simulations, we implement the model on an adaptive mesh with 15 vertical layers as follows: (i) a time interval is defined over which the change in ice cap extent is small relative to the size of the ice cap; (ii) within this interval, only vertical mesh deformation is permitted in solving the free surface equation (equation (4) in the supporting information); (iii) outside this interval, a new surface topography is extracted from the model and extrapolated (if necessary) to define the new ice margin; (iv) the new margin and surface topography are used to construct a new mesh; (v) state variables are interpolated from the old mesh to the new mesh; and (vi) the simulation is initialized on the new mesh with the interpolated variables from the previous run as the initial condition.

In the retreating glacier case, no extrapolation of the surface topography is needed. A residual ice thickness of 10 m is retained in areas evacuated by the glacier. The remeshing step consists only of redefining a new glacier margin by removing the residual ice. In the advancing case, extrapolation is needed since the surface topography outside of the glacier margin is not within the model domain. Extrapolation of the surface topography is done using the MATLAB grid data function (v4 method), and a new margin is defined as the computed 10 m contour of glacier thickness. This method is not mass conserving, so we add a check on mass

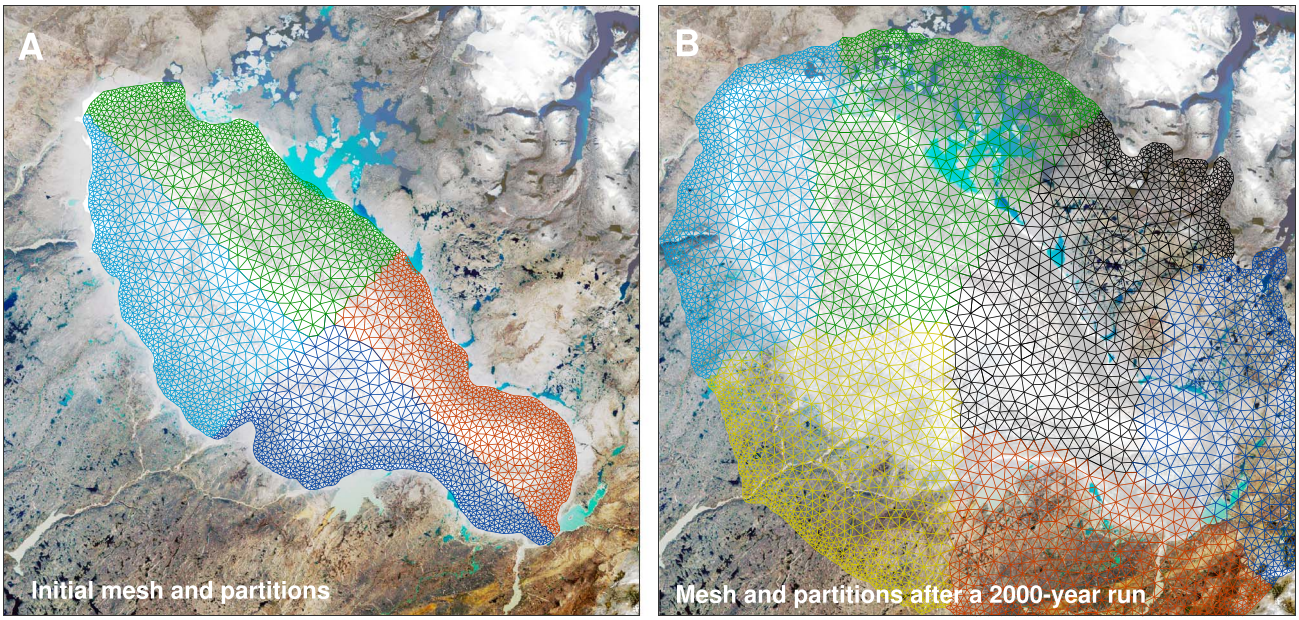

Figure 3. Example of adaptive mesh and partitioning (colors) for parallel computing. (a) Initial mesh. (b) Mesh after 2000 model years with a positive mass balance.

conservation in order to quantify the error introduced by the extrapolation. For this purpose we integrate the total mass flux across the lateral boundary for each remeshing time step to obtain a total mass loss across the ice cap margin prior to remeshing M_l (Gt). We also compute the mean mass balance M_b (kg m^{-2} yr^{-1}) at the edge of the ice cap. We ensure that

$$M_{\text{new}} - M_{\text{old}} \simeq M_l + \frac{S_{\text{new}} - S_{\text{old}}}{2} \times \Delta t \times M_b, \tag{12}$$

where M_{new} and S_{new} are, respectively, the total mass (Gt) and surface area (m^2) of the ice sheet after remeshing, M_{old} and S_{old} are, respectively, the total mass (Gt) and surface area (m^2) of the ice sheet before remeshing, and Δt is the elapsed time between two remeshings. Quantity $(S_{\text{new}} - S_{\text{old}})/2$ is the mean surface area outside the model boundary in the time interval Δt. The error associated with the extrapolation process is then estimated by comparing the two sides of equation (12). We find that this error does not exceed 1% of the total ice cap mass, even after several millennia.

The method above allows us to optimize the number of nodes and partitions for parallel computing as a function of ice cap geometry (Figure 3). It also enables mesh refinements in the vicinity of complex structures, such as canyons or valleys (Figure 3b, northeast sector of the ice cap).

4. Model Setup

4.1. Mass Balance

4.1.1. Climate Forcing: Temperature and Precipitation

Comparison between measured in situ winter mass balance on Barnes [*Hooke et al.*, 1987; *Holdsworth and Hooke*, 1977; *Loken and Sagar*, 1967] and winter precipitation recorded at the surrounding weather stations reveals a poor correlation for the 13 years of available data (gridded data [*Hutchinson et al.*, 2009]: $R^2 = 0.3$; Clyde River: $R^2 = 0.21$; and Dewar Lakes: $R^2 = 0.21$). The poor correlation could be explained by the notorious difficulty of measuring Arctic precipitation due to gauge undercatch and the need to correct gauge biases [*Mekis and Hogg*, 1999]. In our case, the use of a time-dependent versus constant precipitation factor P_{ref} does not improve the modeled annual net mass balance compared to available mass balance measurements. Therefore, we choose to fix the precipitation factor P_{ref} in time and treat it as an adjustable parameter. P_{ref} represents the mean annual precipitation at the northwest extremity of Barnes. Although the three temperature time series (see section 2.2) are well correlated with one another, the best agreement between modeled and measured mass balance is obtained using the mean temperature of the Dewar Lakes and Clyde River

Table 1. Mass Balance Model Parameters

Parameter	Symbol	Mean ± Standard Deviation	Units
Air temperature lapse rate	dT/dz	6.2×10^{-3} (fixed)	$K\,m^{-1}$
Rain-snow precipitation threshold	T_p	275.15 (fixed)	K
Threshold temperature for melting	T_m	270.4 (fixed)	K
Degree-day factor for ice	f_{ice}	$4.52 \pm 0.2 \times 10^{-3}$	$kg\,m^{-2}\,yr^{-1}\,K^{-1}$
Degree-day factor for snow	f_{snow}	$1.56 \pm 0.2 \times 10^{-3}$	$kg\,m^{-2}\,yr^{-1}\,K^{-1}$
Precipitation factor	P_{ref}	$1.2 \pm 0.2 \times 10^{-1}$	$kg\,m^{-2}\,yr^{-1}$
Precipitation lapse rate	dP/dz	$4.0 \pm 0.4 \times 10^{-4}$	$kg\,m^{-2}\,yr^{-1}\,m^{-1}$
Longitudinal precipitation factor	f_p	$1.2 \pm 0.4 \times 10^{-2}$	km^{-1}
Eastern limit of longitudinal precipitation gradient	d_0	36.6 ± 5.6	km
Refreezing factor	f_R	$2.0 \pm 0.9 \times 10^{-1}$	-

stations. We use this mean as our reference air temperature time series for the mass balance model calibration, described in section 4.1.2.

4.1.2. Model Parameter Estimation

Mass balance model parameters are summarized in Table 1. Among these parameters, six are evaluated by estimating a probability density function (PDF) calculated from the differences between modeled and measured variables using a gridded search over the parameter space (with ~10^6 parameter combinations). This PDF is equal to the product of the probability P associated with each data set for which a covariance matrix representing data uncertainty is written:

$$P \propto \exp\left(-0.5(\boldsymbol{m}-\boldsymbol{d})\boldsymbol{C}^{-1}(\boldsymbol{m}-\boldsymbol{d})^{T}\right) \tag{13}$$

with P being the probability density, **m** the vector of modeled values, **d** the data, and **C** the covariance matrix that describes uncertainty of the data, respectively. The PDF has been computed for each parameter using the following data: (i) mean geodetic mass balance over the whole ice cap between 1960–1995, 1960–2007, and 1960–2010 [*Gardner et al.*, 2012], (ii) the mass balance-elevation profile on the south dome between 1975 and 1984 [*Hooke et al.*, 1987], (iii) mean net mass balance in each of the five zones (see Figure 2) in 1966 [*Loken and Sagar*, 1967], (iv) the winter mass balance-elevation profile in 1965 and 1966 for Zones 1 and 4 [*Loken and Sagar*, 1967], (v) the mass balance-elevation profile in 1964 (Zones 1 and 4) and 1965 (Zone 1) [*Loken and Sagar*, 1967], and (vi) mean net balance between 1962 and 2010 at Sagar's camp (see Figure 2). During a flyover in July 2010, we observed stakes from the camp established in 1962 [*Sagar*, 1966], indicating roughly balanced conditions at the camp location on average from 1962 to 2010. The near-surface lapse rates over Canadian Arctic glaciers have been found to deviate from the moist adiabatic lapse rate [*Gardner et al.*, 2009], but little information is available specifically for Barnes. Parameter estimation has been done assuming a mean temperature lapse rate $dT/dz = -6.2 \times 10^{-3}\,K\,m^{-1}$ based on the comparison between temperature recorded at Clyde River and Barnes at 1073 m asl during summer 1962, 1963, and 1964 [*Sagar*, 1966]. The snow-rain threshold temperature T_p is fixed at 275.15 K. These two parameters have a similar impact on the modeled mass balance as the melt and precipitation factors, making it difficult to constrain both simultaneously. We therefore fix dT/dz and T_p. The threshold for melting (T_m) is estimated by matching the modeled melt season length at the summit of Barnes as estimated from microwave remote sensing [*Dupont et al.*, 2012]. Using our fixed temperature lapse rate gives $T_m = 270.4$ K, a reasonable value considering we use daily mean air temperature to compute the number of PDD [*Senese et al.*, 2014] (maximum daily temperature can exceed 273.15 K even for daily mean temperature less than 273.15 K). Here we assume the 1960 ice cap geometry.

4.2. Thermomechanical Model

4.2.1. Diagnostic Simulations

4.2.1.1. Strategy for 1960 Initial State

The initial mesh (see Figure 3a) has been constructed using bedrock topography interpolated from NASA IceBridge radar tracks with kriging (Figure 2b) and surface topography from the Canadian Digital Elevation Model (CDEM) based on aerial stereo images taken in 1960. To produce an initial state for the transient simulations as well as analyze the current state of Barnes, we first solve the thermomechanical problem with a steady state temperature field and basal sliding computed from the friction parameter β obtained by

inversion. We assume no Pleistocene ice layer. We proceed following these steps: (i) surface topography is relaxed during a 20 year spin-up assuming zero net balance conditions and no sliding. In this first step, the dynamics model is coupled to a steady state temperature field where surface temperature (coefficients a and b in equation (12) in the supporting information) and geothermal heat flux (f_g in equation (14) in the supplementary material) are calibrated to match the borehole temperature measurements from the south dome. The best match is obtained for $f_g = 2.8 \times 10^{-2}$ W m^{-2}. The spatial distribution of firn (presence/absence) and a mean air temperature corresponding to a modeled zero net balance state is also assumed. (ii) The relaxed surface is then used to infer the friction parameter β (described below). The steady state temperature field is recalculated as the velocity field evolves due to the iterative updates to β during the inversion.

We invert for the friction parameter assuming a linear sliding law ($m = 1$ in equation (13) of the supporting information) and by minimizing a cost function with a regularization term using a control inverse method [*Gagliardini et al*., 2013; *Gillet-Chaulet et al*., 2012]. The cost function is based on the misfit between the model and two independent data sets: (i) the InSAR surface velocity field $u_{\mathrm{InSAR}}^{\mathrm{obs}}$ and (ii) the vertical component of the surface-normal velocity u_{Nz}^{obs}:

$$J_0 = \gamma_1 \int_{\Gamma_s} \frac{1}{2} \left(\left(|u_{Nz}| - |u_{Nz}^{\mathrm{obs}}| \right) \right)^2 \mathrm{d}\Gamma + \gamma_2 \int_{\Gamma_s} \frac{1}{2} \left(\left(|u_{\mathrm{InSAR}}| - |u_{\mathrm{InSAR}}^{\mathrm{obs}}| \right) \right)^2 \mathrm{d}\Gamma + \lambda J_{\mathrm{reg}}, \tag{14}$$

$$J_{\mathrm{reg}} = \frac{1}{2} \int_{\Gamma_b} \left(\left(\frac{\partial \beta}{\partial x} \right)^2 + \left(\frac{\partial \beta}{\partial y} \right)^2 \right) \mathrm{d}\Gamma, \int_{\Gamma_b} \left(\left(\frac{\partial \beta}{\partial x} \right)^2 + \left(\frac{\partial \beta}{\partial y} \right)^2 \right) \mathrm{d}\Gamma, \tag{15}$$

where $u_{Nz} = (\boldsymbol{u} \cdot \boldsymbol{N})Nz$ with $\mathbf{N} = (N_x, N_y, N_z)$ the unit vector normal to the surface, Γ_s is the surface boundary, J_{reg} is the regularization term, Γ_b is the bedrock surface boundary, λ is a positive number, and γ_1 and γ_2 are positive weighting factors. u_{Nz}^{obs} is obtained by removing the mean modeled 1960–2010 mass balance from the elevation change rate measured by digital elevation model (DEM) differencing over the same period [*Gardner et al*., 2012]. u_{InSAR} is obtained using the satellite-look direction vector $\mathbf{N}_{\mathrm{sat}}$ with $u_{\mathrm{InSAR}} = \boldsymbol{u} \cdot \boldsymbol{N}_{\mathrm{sat}}$. Uncertainties on $u_{\mathrm{InSAR}}^{\mathrm{obs}}$ are estimated to be less than 0.5 m yr^{-1}.

4.2.1.2. Estimating the Initial PIL Thickness

We assume the influence of the PIL can be quantified as a function of its thickness and its characteristic enhancement factor E (see equation (6) in the supporting information) using a simple two-layer slab approximation. We express the thickness H_p (m) of the PIL as a function of the tangential velocity at the top of this layer v_p (m s^{-1}):

$$H_p = H_{\mathrm{ice}} - \left(H_{\mathrm{ice}}^{n+1} - \frac{H^n (n+1) v_p}{2A(E-1)\tau_b^n} \right)^{\frac{1}{n+1}}, \tag{16}$$

where H_{ice} is the total ice thickness (m), A is the flow-law rate factor (s^{-1} Pa^{-3}), τ_b is the basal shear stress, and n is Glen's exponent.

To estimate the value of E, we compute the thickness of the PIL along a profile on the south dome where surface velocities and temperatures are known (Figure 2). We assume that the velocity v_p at the top of the PIL is equal to the difference between the measured surface velocities (blue dots, Figure 4) and the modeled surface velocities assuming no sliding and no enhancement (red curve on Figure 4). Using equation (16) we obtain different PIL thickness profiles for different values of enhancement E. These profiles can then be compared to an independent estimate of the PIL thickness to determine the best value of E.

The PIL thickness distributed across the whole ice cap can then be estimated again using equation (16), with the rate factor A calculated from the modeled basal temperature, the basal drag computed using the ice flow model, and the value of E previously computed on the south dome profile. However, making the assumption that v_p is equal to the inferred basal sliding velocity v_b leads to unrealistic PIL thickness where either v_b is too high or the basal drag too low. We therefore introduce a maximum PIL thickness, H_{pmax}, set to the lesser of 80 m or the total ice thickness. We can then define v_{pmax}, the maximum velocity at the top of the PIL:

$$v_{\mathrm{pmax}} = \frac{2\tau_b^n (E-1) A}{n+1} \left(H_{\mathrm{ice}} - \frac{\left(H_{\mathrm{ice}} - H_{\mathrm{pmax}} \right)^{n+1}}{H_{\mathrm{ice}}^n} \right). \tag{17}$$

The maximum PIL thickness reported by *Hooke* [1976] on the south dome is 40 m, becoming thinner toward the center of the ice cap [*Hooke and Hanson*, 1986]. We assume $H_{\mathrm{pmax}} = 80$ m as a reasonable global limit

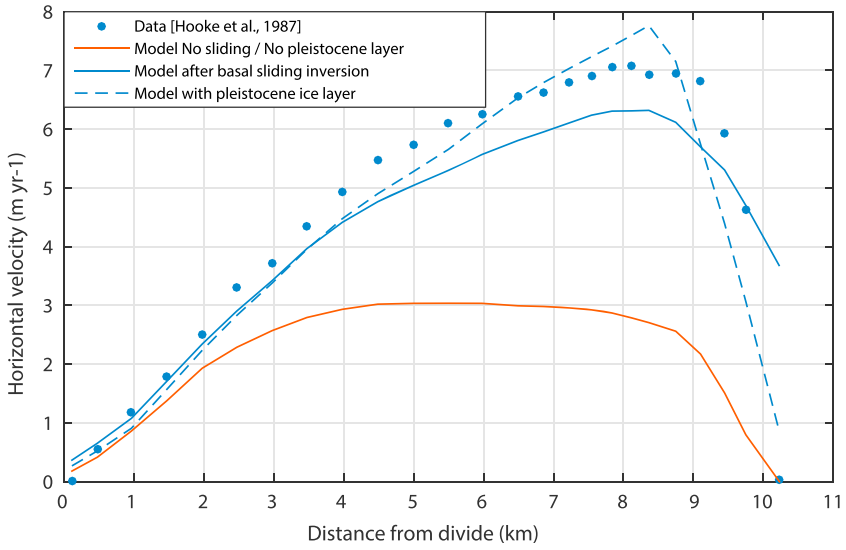

Figure 4. Measured and modeled surface velocities along a profile on the south dome (see Figure 1, blue line).

considering that the 40 m constraint applies only to a single profile. If v_b exceeds v_{pmax}, sliding must occur with a velocity equal to $v_b - v_{pmax}$ This condition provides a criterion for separating true sliding from enhanced basal deformation, which was initially lumped into the inversion for sliding parameter β. The estimated distribution of PIL thickness is then used to initialize the geometry of the PIL body described in section 3.2. A final value of β is obtained by an inversion that includes the PIL body in the model.

4.2.2. Prognostic Simulations

Starting from the 1960 initial state, determined using the methods described above, prognostic simulations are run using a time step of 2 years and driven with a 2 year mean mass balance. The margin of the ice cap and mesh are updated every 20 years (see section 3.4). The duration of these simulations depends on the disappearance date of the ice cap. Simulations were limited to 2000 or 4000 years, depending on model parameters, in the case of ice cap survival.

5. Results

5.1. Mass Balance

Mean parameter values and their associated standard deviations obtained by the fitting method described above are summarized in Table 1. Degree-day factors are low in comparison with other values from the literature [*Hock*, 2003] because we use a threshold for melting that differs from the commonly used 273.15 K (270.4 K here); the use of $T_m = 273.15$ K would give $f_{ice} = 8.0 \times 10^{-3}$ kg m^{-2} yr^{-1} K^{-1} and $f_{snow} = 5.6 \times 10^{-3}$ kg m^{-2} yr^{-1} K^{-1}, in better agreement with commonly reported values.

Mass balance modeling results are shown in Figures 5 and 6. Over the period 1960–2010 the mass balance of Barnes was mostly negative with just a few positive mass balance years during the 1970s (Figures 5b and 6b) and a steady decrease after 1980. Mass balance estimated back to 1870 using the CRUTEM4 data (see inset, Figure 5b) exhibits a short period of balanced conditions at the end of the nineteenth century. We estimate that Barnes lost about 340 Gt of ice (17% of its mass) from 1900 to 2010.

Due to the precipitation increase toward the southeast, mean surface mass balance (1960–2010) at the top of the south dome is positive despite its lower elevation (Figure 5a). This surface mass balance pattern is confirmed by satellite snowline observations at the end of summer [*Andrews*, 2002] and by altimetry measurements that show little change on the south dome compared to other similar elevations across Barnes [*Gardner et al.*, 2012], meaning that the mass balance in this area has to be positive to compensate the negative surface-normal velocity at the divide. For example, the modeled Equilibrium Line Altitude (ELA) closely matches the configuration of the snow line in August 2010 from Landsat imagery (Figure 5a). Evolution of the ELA (Figure 5a) shows that Barnes has nearly lost its accumulation area over the last 10 years.

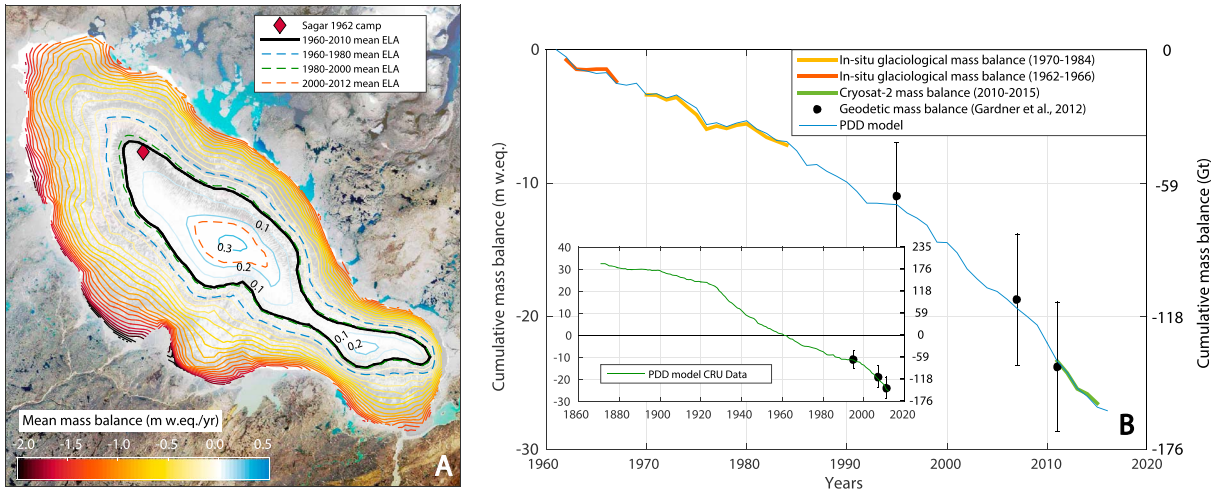

Figure 5. (a) Mean surface mass balance modeled over the 1960–2010 period. The black line shows the mean Equilibrium Line Altitude (ELA) over the same period. Red diamond is the location of the Sagar 1962 camp [*Sagar*, 1966], visible in 2010. (b) Modeled cumulative mass balance of Barnes compared to in situ [*Hooke et al*., 1987; *Loken and Sagar*, 1967] and global geodetic data [*Gray et al*., 2015; *Gardner et al*., 2012]. The inset shows modeled cumulative mass balance using CRUTEM4 data from Greenland (see Figure 1).

Currently, accumulation only occurs around the top of central dome in the form of superimposed ice. Figures 6a, 6c, and 6d compare different modeled and measured annual or winter mass balance profiles for different dates and zones as a function of elevation. Results are in reasonable agreement with measurements, thus providing a qualitative validation of the mass balance model in terms of spatial and temporal variability.

5.2. Diagnostic Simulations

5.2.1. Dynamical and Thermal Regime

The mean 1960–2010 surface mass balance (Figure 5a) subtracted from the measured rate of elevation change (Figure 7a) over the same period gives the vertical component of the surface-normal velocity, u_{Nz}^{obs}. This is the dynamic component of the elevation change (Figure 7b). We compute an anomaly field of u_{Nz}^{obs} (Figure 7c) by adding to u_{Nz}^{obs} the surface mass balance that best fits the original u_{Nz}^{obs} (Figure 7b) to highlight flow anomalies where the vertical subsidence or emergence differs from that required to maintain a steady ice cap surface geometry. The anomaly field highlights two zones along the southwest margin of the ice cap where the current surface topography is not in equilibrium with the current dynamics, likely due to changes in basal conditions.

Inversion results using u_{Nz}^{obs} only (Method 1, $\gamma_1 = 1.0$ and $\gamma_2 = 0.0$, see equation (14)), InSAR line-of-sight velocities only (Method 2, $\gamma_1 = 0.0$ and $\gamma_2 = 1.0$), or both (with $\gamma_1 = 1.0$ and $\gamma_2 = 0.01$) are shown in Figures 8a–8c, respectively. The different surface velocity fields obtained using Methods 1 and 2 (Figures 8a and 8b) are in good agreement with each other, thus validating the approach of using elevation change and mass balance to constrain dynamics. The similarity of results between Methods 1 and 2 was not a foregone conclusion, as the InSAR data represent surface displacements over a 24 h period, whereas the elevation change method reflects mean ice flow over 60 years. Discrepancies between the two results are observed in the north and south sectors of Barnes, mainly due to the fact that flow is perpendicular to the satellite-look direction in this region (see Figure 9), and the InSAR data therefore cannot constrain the inversion there. The inversion using the InSAR data also leads to an unrealistically sharp transition between sliding and no sliding conditions at the divide in the northern region of the ice cap. The advantage of Method 1 is its independence of flow direction, which allows us to constrain the inversion everywhere. For example, comparison with in situ velocity measurements on the south dome lobe [*Loken et al*., 1968; G. Holdsworth, personal communication, 2015] shows that we obtain better results with Method 1 than with Method 2 (Figure 8f). However, Method 1 also suffers from low sensitivity of normal velocity to surface flow magnitude because velocity vectors are roughly parallel to the surface. The use of modeled surface mass balance also introduces additional uncertainty. We therefore combine the two methods to obtain the reference velocity field in Figure 8c (see Figures 8 and 9).

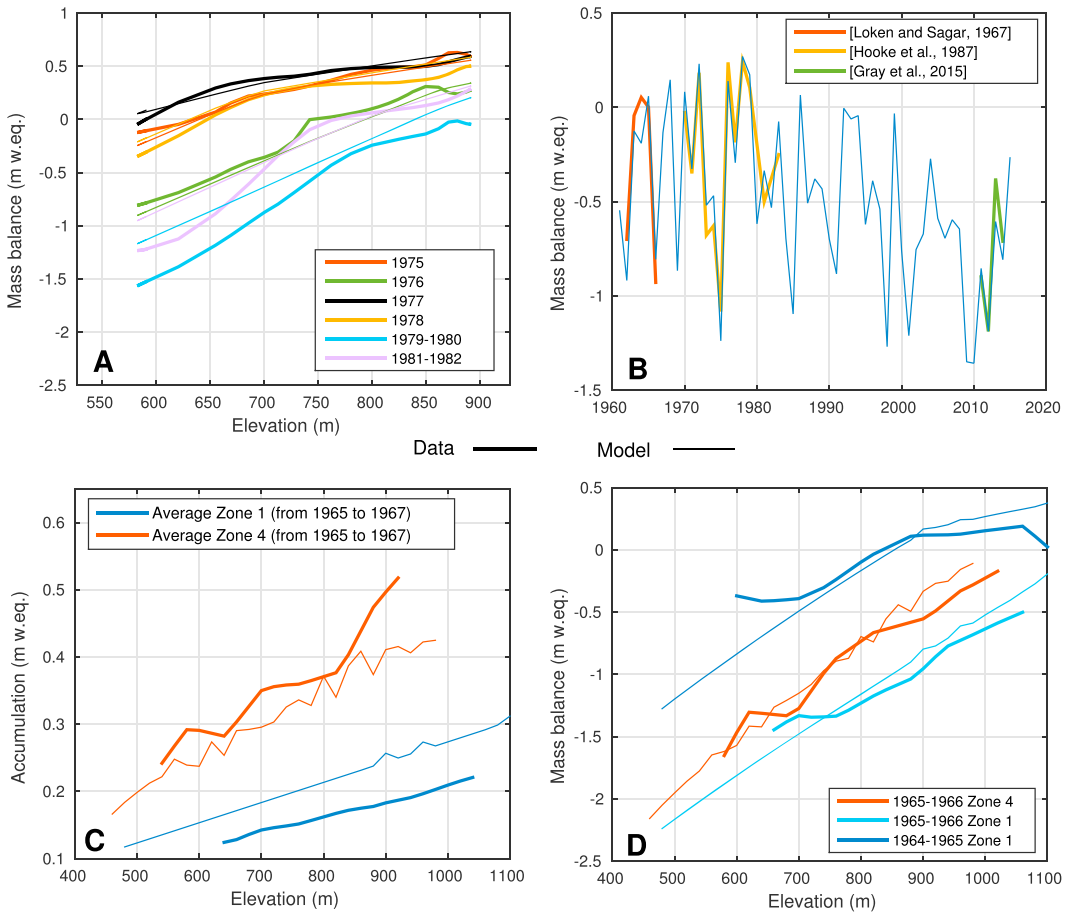

Figure 6. Modeled (thin lines) and measured (thick lines) mass balance. (a) Modeled and measured surface mass balance for different years along the south dome profile (blue line in Figure 2) [*Hooke et al.*, 1987]. (b) Modeled and measured annual mass balance over the whole ice cap. Measurements on south dome profile were extrapolated across the whole ice cap by using the mean ratio between modeled mass balance on the profile and modeled mass balance over the whole ice cap. (c) Modeled and measured mean winter accumulation as a function of elevation in Zones 1 and 4 (see Figure 2 measured) [*Loken and Sagar*, 1967]. (d) Modeled and measured mean surface mass balance as a function of elevation in Zones 1 and 4 (see Figure 1) [*Loken and Sagar*, 1967].

Results have also been compared with horizontal velocities obtained using speckle tracking on ALOS-PALSAR satellite imagery (Figure 8e) [*Van Wychen et al.*, 2015] on a profile located on Lobe 1 (dashed line in Figures 8a and 8b). Speckle tracking uncertainty is about 5 m yr^{-1}.

The dynamics revealed by the inversion shows that Lobes 1 and 2 (see bold white numbers in Figure 8c) are maintained by enhanced sliding that is still active today. The topographic adjustment associated with Sliding Area 1 (same bold white numbers in Figure 8c) has reached a steady state in its central region, but a new smaller sliding zone to the east has appeared more recently, as indicated by a subsidence velocity anomaly in Figure 7c (circled area 2). This anomaly is linked to a smaller and younger sliding zone clearly visible in the InSAR inversion (Figure 8b) as a high velocity patch located a few kilometers east of the main sliding zone. Topographic adjustment in Sliding Area 2 seems to still experience a surface lowering linked to the appearance of the sliding instability (Figure 7c). Lobe 4 was likely also formed by enhanced sliding but has not been active since at least 1960. A positive normal velocity anomaly is clearly visible in Figure 7c (circled area 1) in the zone previously affected by sliding.

Differences between the modeled and observed thermal regime are investigated next. Modeled basal temperatures are shown in Figure 10 and suggest that Barnes is mostly cold based, with a few temperate areas situated near the ice margin. The largest modeled temperate area (under Lobe 4) is partially a consequence of the positive anomaly in vertical velocity due to the transient adjustment of surface topography. This anomaly

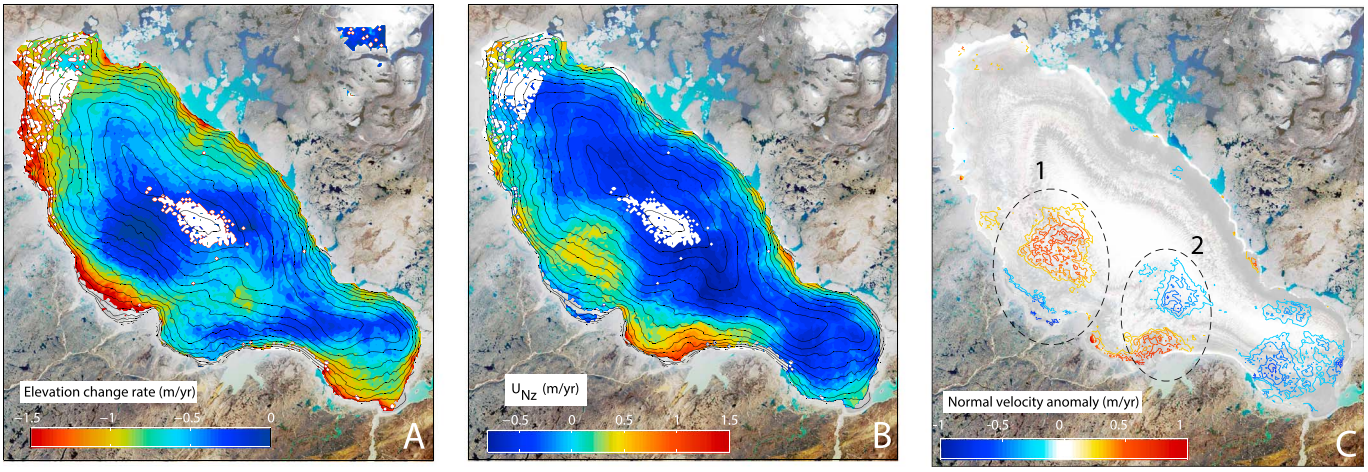

Figure 7. (a) Observed rate of elevation change between 1960 and 2010 (adapted from *Gardner et al.* [2012]). (b) Vertical component of the surface-normal velocity (u_{Nz}^{obs}) obtained by subtracting the modeled 1960–2010 mean mass balance (Figure 5a) from the observed rate of elevation change (Figure 7a). (c) u_{Nz}^{obs} anomaly, excessive surface lowering in blue, excessive surface uplift in red (see text).

yields incorrect modeled temperatures under steady state assumptions by reducing the penetration of cold surface temperatures to the bed. Comparisons of modeled and measured borehole temperatures are shown in Figures 10b and 10c. The surface temperature is tuned such that the model agrees with the deepest measured temperatures. The differences between borehole T020 and T061 reflect different surface conditions associated with the transition between the ablation and accumulation zones, where warmer surface temperatures occur above the ELA due to meltwater refreezing in the firn [e.g., *Hooke et al.*, 1983; *Gilbert et al.*, 2012]. The difference between the modeled steady temperature and measured temperature profile in borehole T020 is due to the surface cooling associated with the reduction of firn thickness [*Gilbert et al.*, 2012] since the Little Ice Age (today the firn is almost nonexistent). *Hooke et al.* [1980] also attributed this cooling to climatic warming resulting in an increase in superimposed ice and hence a decrease in meltwater penetration (and associated latent heat release) into the underlying firn. Large discrepancies between modeled and measured temperatures in borehole B4 are mainly due to a locally higher basal heat flux that *Hooke et al.* [1980] attributed to locally higher geothermal flux. The proximity of a temperate sliding zone (Lobe 2 in Figure 8c), however, suggests that borehole B4 may be affected by basal meltwater. Sliding Areas 1 and 2 (Figure 8c) correspond to subfreezing temperatures modeled in Figure 10a, though the bed must be temperate in reality to allow sliding. Borehole measurements in Sliding Area 2 (Figure 10c) confirm the presence of temperate basal ice, which is not captured by the model. Even without accounting for sliding (which produces surface uplift and a positive vertical velocity anomaly in this area which increases steady state basal temperatures), modeled steady state temperatures in Sliding Area 2 are always cold. The flow instability in this zone must therefore be driven by an external energy supply, such as water refreezing near the bed. Another explanation could be the presence of a geothermal flux anomaly as suggested by *Hooke et al.* [1980] in borehole B4, but our numerical experiments show that the basal heat flux must be $1.5 \times 10^{-1}\,\mathrm{W\,m^{-2}}$ to produce temperate basal ice in Sliding Area 2. This value is about twice that found by *Hooke et al.* [1980] and seems unrealistically high considering the proximity of borehole temperature measurements that show a value less than $8.0 \times 10^{-2}\,\mathrm{W\,m^{-2}}$. A value of $1.5 \times 10^{-1}\,\mathrm{W\,m^{-2}}$ is equivalent to the energy supplied by water refreezing at a rate of $1.4 \times 10^{-2}\,\mathrm{kg\,m^{-2}\,yr^{-1}}$. A similar phenomenon is probably occurring in Sliding Area 1. However, Sliding Areas 3, 5, and 7 correspond to temperate zones in our steady state model (Figure 10a), indicating that frictional and strain heating are able to maintain temperate conditions. These sliding zones are therefore stable. Sliding Area 7 appears to be linked to calving in Bieler Lake.

The decrease in basal shear stress associated with the change in surface topography caused by enhanced flow in Sliding Areas 1 and 2 (Figure 8d) appears insufficient to shut down the sliding activity as we would expect in a normal surge [*Clarke et al.*, 1984]. The cause of sliding shutdown in Area 4 remains unclear but hints at episodic flow variations that could be interpreted as surging with a very long active phase [*Murray et al.*, 2003].

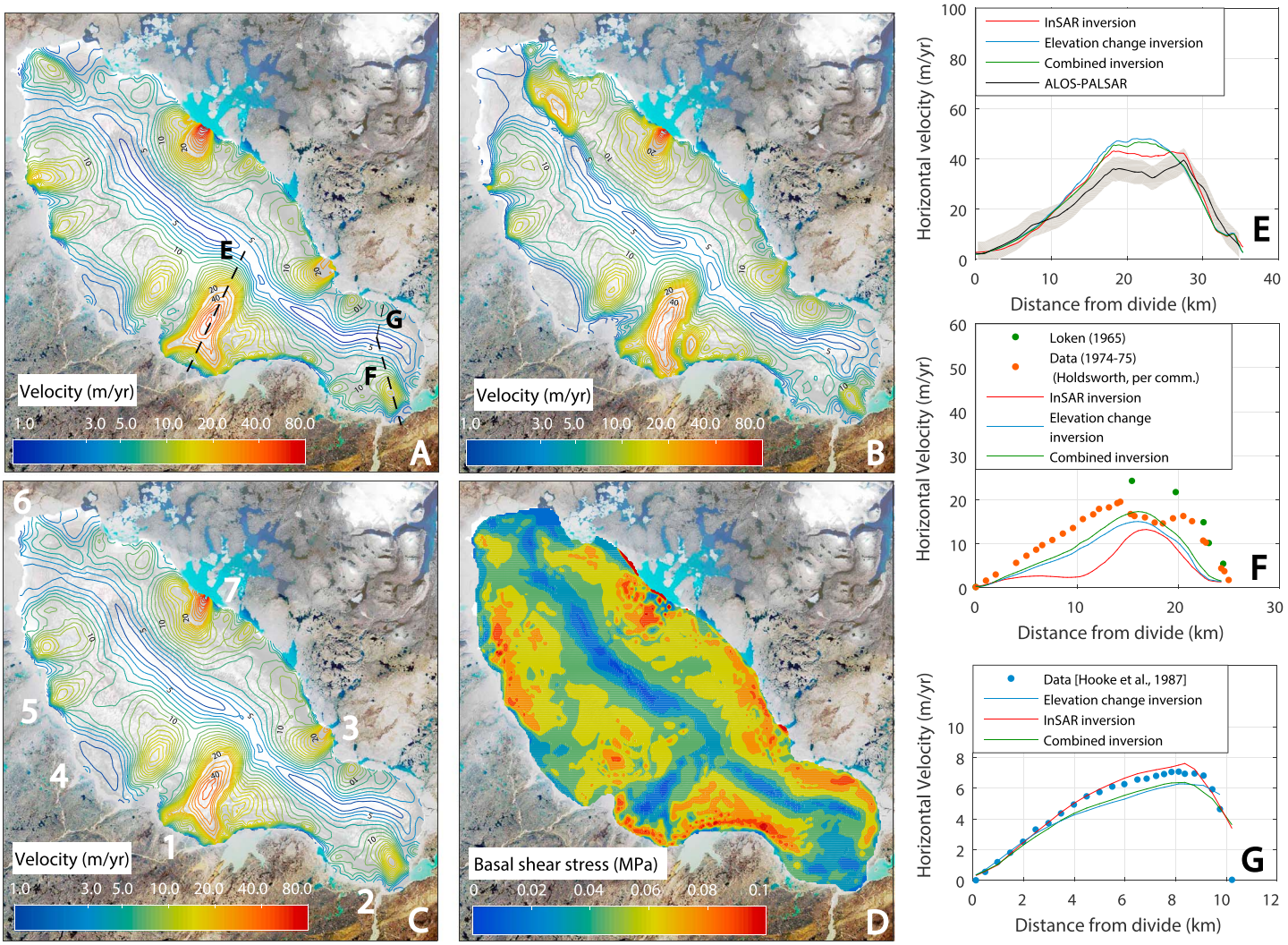

Figure 8. Modeled surface velocity after inversion. Contour intervals are logarithmic for velocities above 20 m yr^{-1} in (a), (b) and (c). (a) Cost function based on elevation change measurements. (b) Cost function based on InSAR measurements. (c) Cost function based on both InSAR and elevation change measurements. (d) Modeled basal shear stress. (e) Modeled and measured [*Van Wychen et al.*, 2015] horizontal velocities along the black dashed profile labeled E in Figure 8a. (f) Modeled and measured (Holdsworth, personal communication, 2015) horizontal velocities along the black dashed profile labeled F in Figure 8a. (g) Modeled and measured [*Hooke et al.*, 1987] horizontal velocities along the black dashed profile labeled G in Figure 8a.

5.2.2. Influence of the Pleistocene Ice

The basal sliding parameter obtained by inversion leads to a doubling of the surface velocities on the north side of the south dome, as compared to a simulation that assumes no sliding. Figure 4 compares simulation results with and without sliding to observations along a profile in this region (blue profile in Figure 2) and establishes that the introduction of sliding leads to better model-data agreement. However, temperature measurements along this same profile (Figure 10b) indicate cold-based ice with temperatures less than −5°C. This contradiction confirms that what we have modeled as sliding here is actually enhanced deformation within the basal ice. Using the method described in section 4.2.1.2. we differentiate the contribution of sliding and enhanced deformation in the PIL. Figure 11b shows the PIL thickness inferred along the south dome profile for different values of the enhancement factor E. We obtain the best match between the position of the Holocene-Pleistocene interface and the 10,000 year isochron with a value of $E = 3.5$. The position of the Holocene-Pleistocene interface was also directly measured in borehole T081 and T061 by *Hooke and Hanson* [1986], and our model matches this measurement for $E = 3.0$ and $E = 2.7$, respectively. These values are comparable to the $E \in [2.5\ 3.0]$ obtained by *Hooke and Hanson* [1986] and $E \sim 3.0$ obtained by *Reeh* [1985] in Greenland from borehole deformation measurements. We chose to use the mean of the three

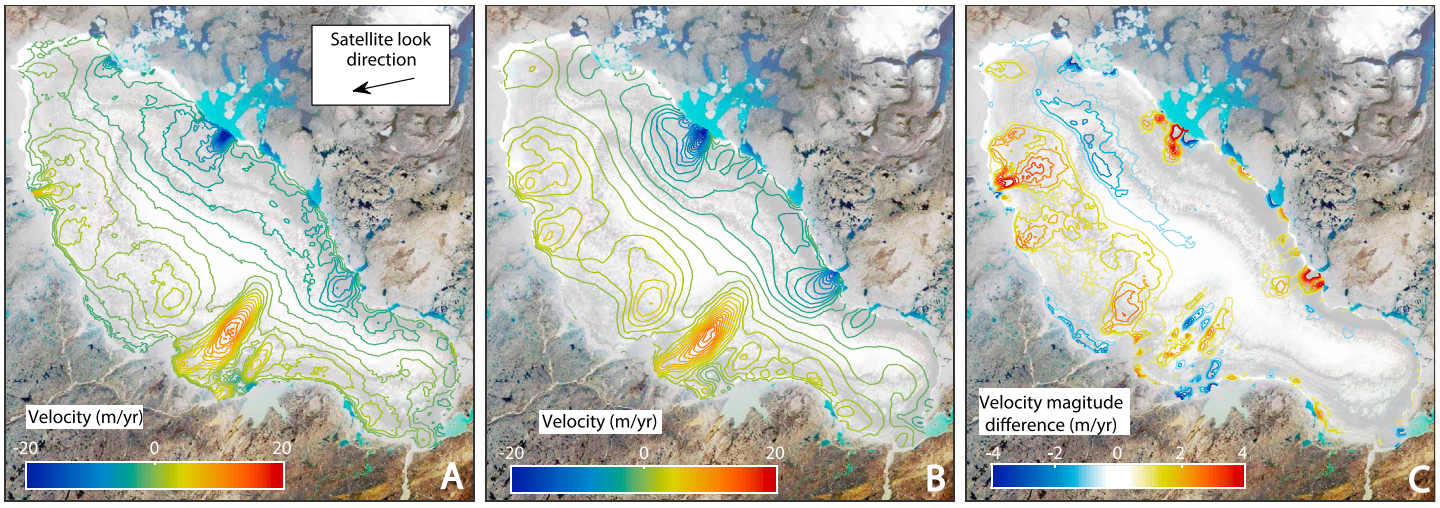

Figure 9. Measured and modeled InSAR satellite-look direction velocities. (a) InSAR velocity measurements using a pair of scenes from 31 March 1996 to 1 April 1996. (b) Modeled velocity in the satellite-look direction. (c) Difference between modeled and measured satellite-look-direction velocities.

values ($E = 3.1$) to compute the PIL thickness across the whole ice cap (Figure 11a), differentiating enhanced basal deformation from sliding (Figure 12). In order to validate our method, we rerun the inversion with the $E = 3.1$ PIL body (see section 3.2.) and obtain a similar sliding velocity field as the one from the two-layer slab approximation (Figure 12a). This result confirms that the two-layer slab model adequately captures the effect of the PIL on surface velocities.

The inferred distribution of Pleistocene ice (Figure 11a) shows a significant area where H_p has been truncated to a maximum thickness of 80 m. The need for this arises from the insensitivity of velocities to PIL thickness where basal shear stress is too low $\left(\frac{\partial H_p}{\partial V_p} \propto \tau_b^{-3}\right)$. These zones have little effect on the flow of the ice cap, because they arise, by definition, where velocities are insensitive to Pleistocene enhancement. Our results are

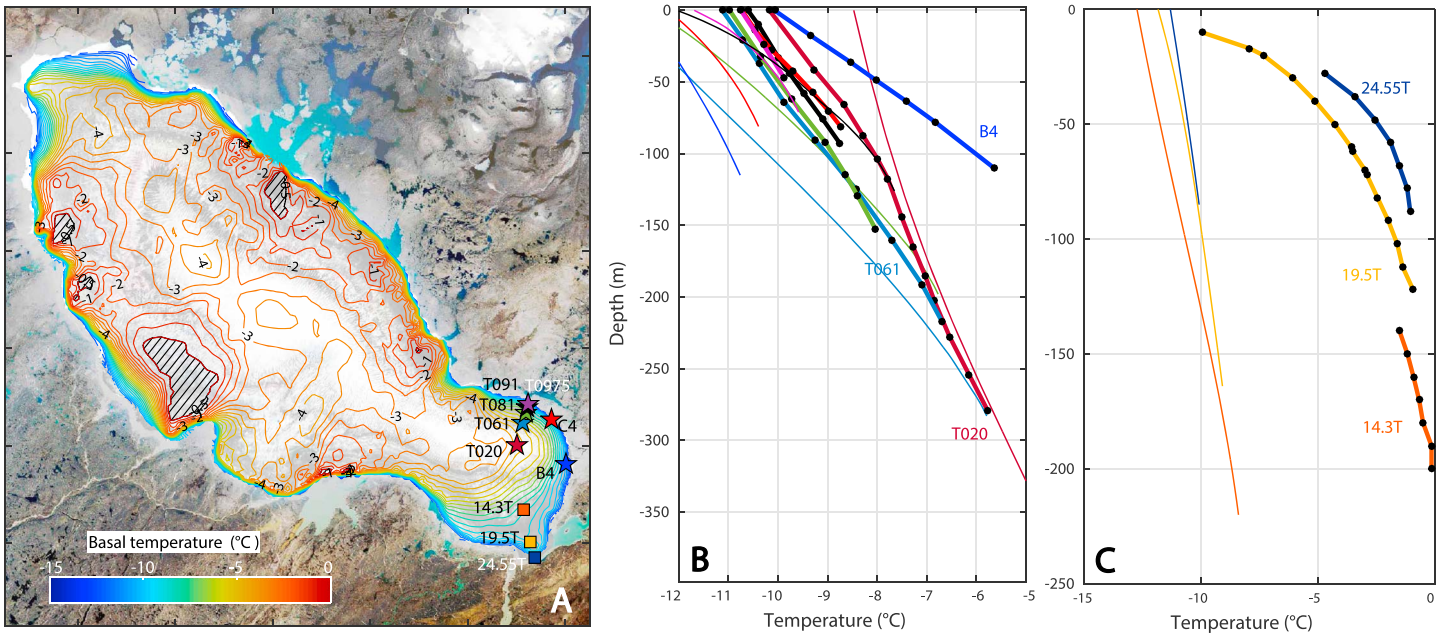

Figure 10. Modeled and measured ice temperatures. (a) Modeled steady state basal temperatures. Hatched areas indicate basal temperatures above −0.5°C. (b) Modeled (fine lines) and measured (bold lines) borehole temperatures [*Hooke et al.*, 1980] along the north side of the south dome (stars in A). (c) Modeled (fine lines) and measured (bold lines) borehole temperatures [*Classen*, 1977] along the south side of the south dome (squares in A).

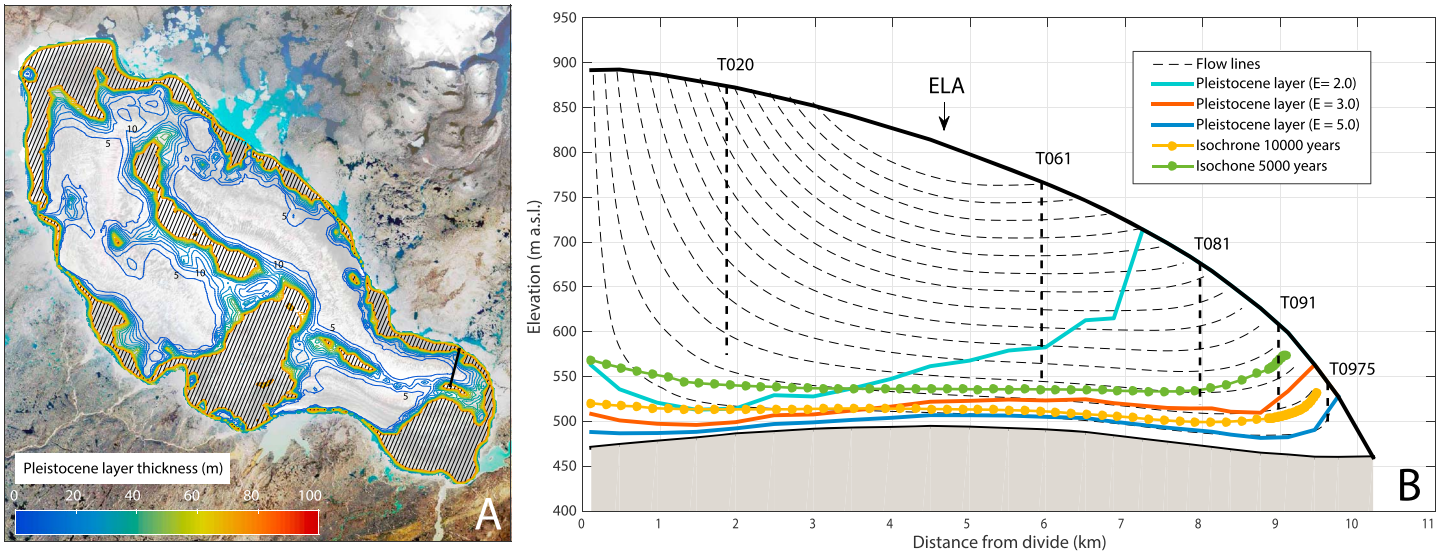

Figure 11. Inferred Pleistocene Ice Layer (PIL) thickness and enhancement factor E. (a) Modeled PIL thickness. Hatched zone shows area where the PIL thickness is set to H_{pmax}. Blank zones are areas with no PIL. (b) Cross section along the south dome (black line in A) showing borehole locations (bold dashed lines), modeled flow lines (thin dashed lines), PIL limits for different enhancement factors E (solid lines), and computed 10,000 year (yellow dots) and 5000 year (green dots) isochrons.

therefore insensitive to the value of H_{pmax} we choose (80 m here). Figure 12b shows that the influence of the PIL is mostly concentrated along the northeastern margin of Barnes and around Sliding Area 2. We interpret dark linear features in the Landsat imagery as the intersection of the ice surface with a specific isochron, meaning that Figures 12c and 12d show that the surface isochrons are perturbed by the flow within two main sliding zones in Lobes 1 and 2, qualitatively confirming the spatial extent of sliding inferred in Figure 12a.

5.3. Prognostic Simulations

The constant climate we use to compute surface mass balance uses a reference annual air temperature cycle that represents the mean annual temperature cycle over the period 1960–2013. This reference cycle is then shifted by ΔT (K) to test the sensitivity of the ice cap to different mean annual temperatures. Sensitivity to precipitation is also tested by multiplying the precipitation factor f_p (equation (3)) by a constant. The basal sliding coefficient and PIL thickness are fixed to the inferred values described in the previous section. No sliding is assumed outside of the 1960 ice cap margin.

5.3.1. Stability of the Current Shape of Barnes Ice Cap

Our experiments reveal that on millennial time scales, the current shape of Barnes is unstable. *Mahaffy* [1976] obtained similar results and concluded that they could probably be explained by the no sliding assumption. Here we suggest that sliding cannot explain the current geometry of the ice cap. The current ice cap configuration is therefore a product of the retreat history of the Laurentide Ice Sheet [*Dyke and Prest*, 1987] (Figure 1) and the generally southwest dipping topography of Baffin Island. Modeled ice cap evolution for four different temperature forcings is shown in Figure 13 with the associated total mass and mean surface mass balance evolution. A warmer climate (Figure 13a) leads to ice cap disappearance in less than 600 years. On this short time scale, ice dynamics has minimal influence and the oblong shape of the ice cap is therefore preserved. A cooler climate (Figures 13b–13d) leads to preferential ice cap advance to the northeast and, if the cooling is sufficient, to the southwest (perpendicular to the longitudinal axis of Barnes), resulting in a more radially symmetric ice cap. The rapid retreat of the northwest and southeast margins [*Briner et al.*, 2009; *Dyke and Prest*, 1987], by comparison, is due to the inherited geometry of the retreating Laurentide Ice Sheet and the dynamic inactivity of these reaches.

The model experiment in Figure 13 also reveals that the ice divide tends to migrate northeast. Figure 13b is an example in which Barnes approaches a steady state but with an up-slope (northeast) migration of the divide (see Figure 13b inset). This illustrates that the southwest margin of Barnes is more subjected to retreat than the northeast margin, in accordance with the lack of evidence for past moraines on the northeast side of

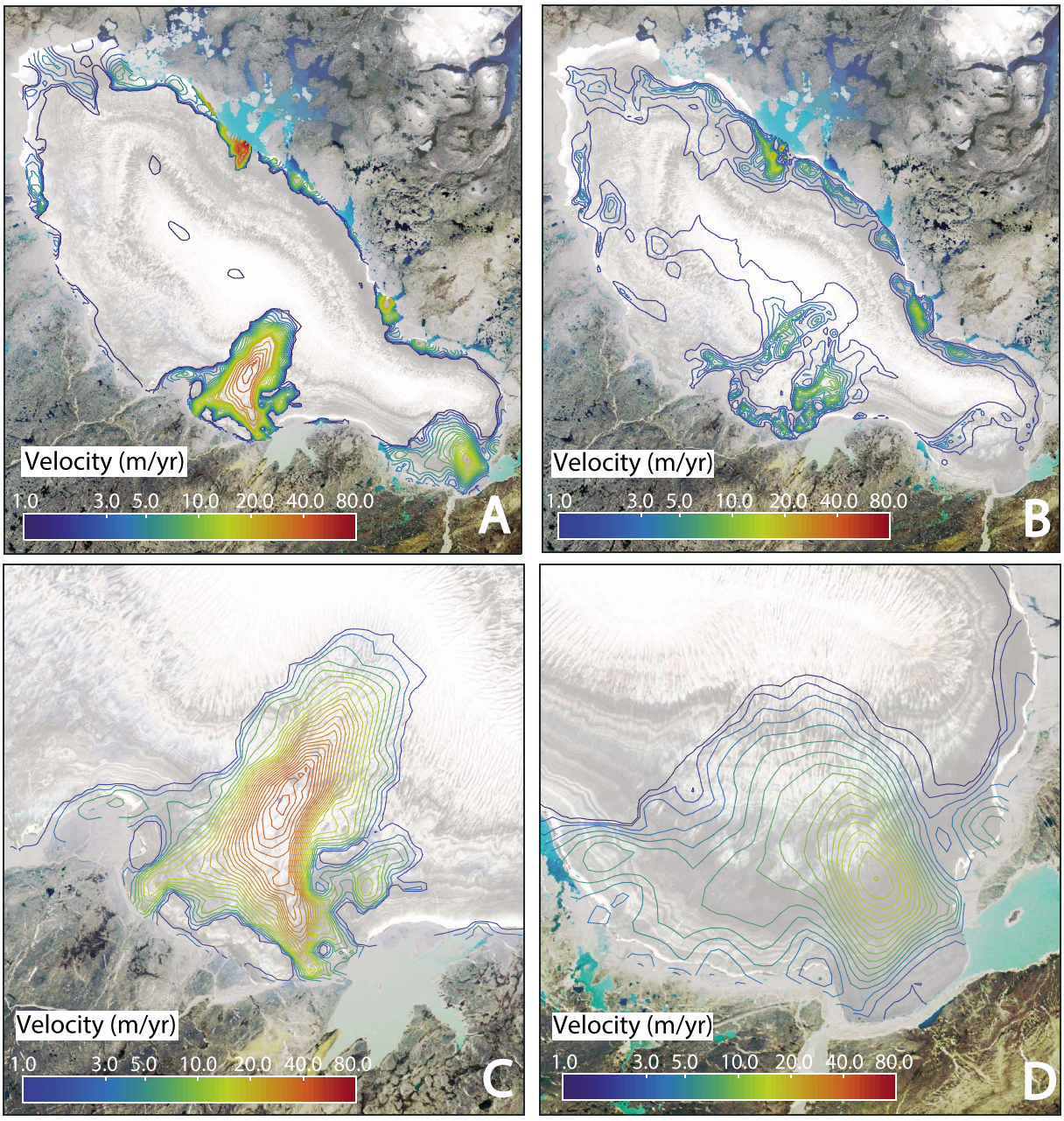

Figure 12. Sliding velocities and enhanced deformation at the base of Barnes Ice Cap obtained using the two-layer slab model and inversion of the sliding parameter β. (a) Final modeled sliding velocity. (b) Modeled velocity at the top of the PIL. (c, d) Close-up of the two main sliding zones in A.

Barnes between the current margin and the "Cockburn end-moraine system" (~8 ka B.P.) [*Andrews and Ives*, 1978]. The northeast margin has been stable for at least 4000 years [*Andrews and Barnett*, 1979; *Andrews and Ives*, 1978], except for a slight advance during the Little Ice Age [*Hooke*, 1976]. The southwest margin, by contrast, has retreated significantly [*Andrews and Barnett*, 1979]. This behavior could be explained by the bedrock, which slopes southwest (see Figure 13b inset) and contributes to the ice cap asymmetry.

We investigate the influence of bedrock slope by performing two additional simulations, assuming either flat or uniformly sloping bedrock and applying the same climatic conditions starting from the 1960 initial state. To simplify the interpretation of the results we omit the PIL and sliding. Inclined bedrock leads to an asymmetric ice cap (Figure 14b) and thus an increase in the ice flux normal to the surface on the up-slope side,

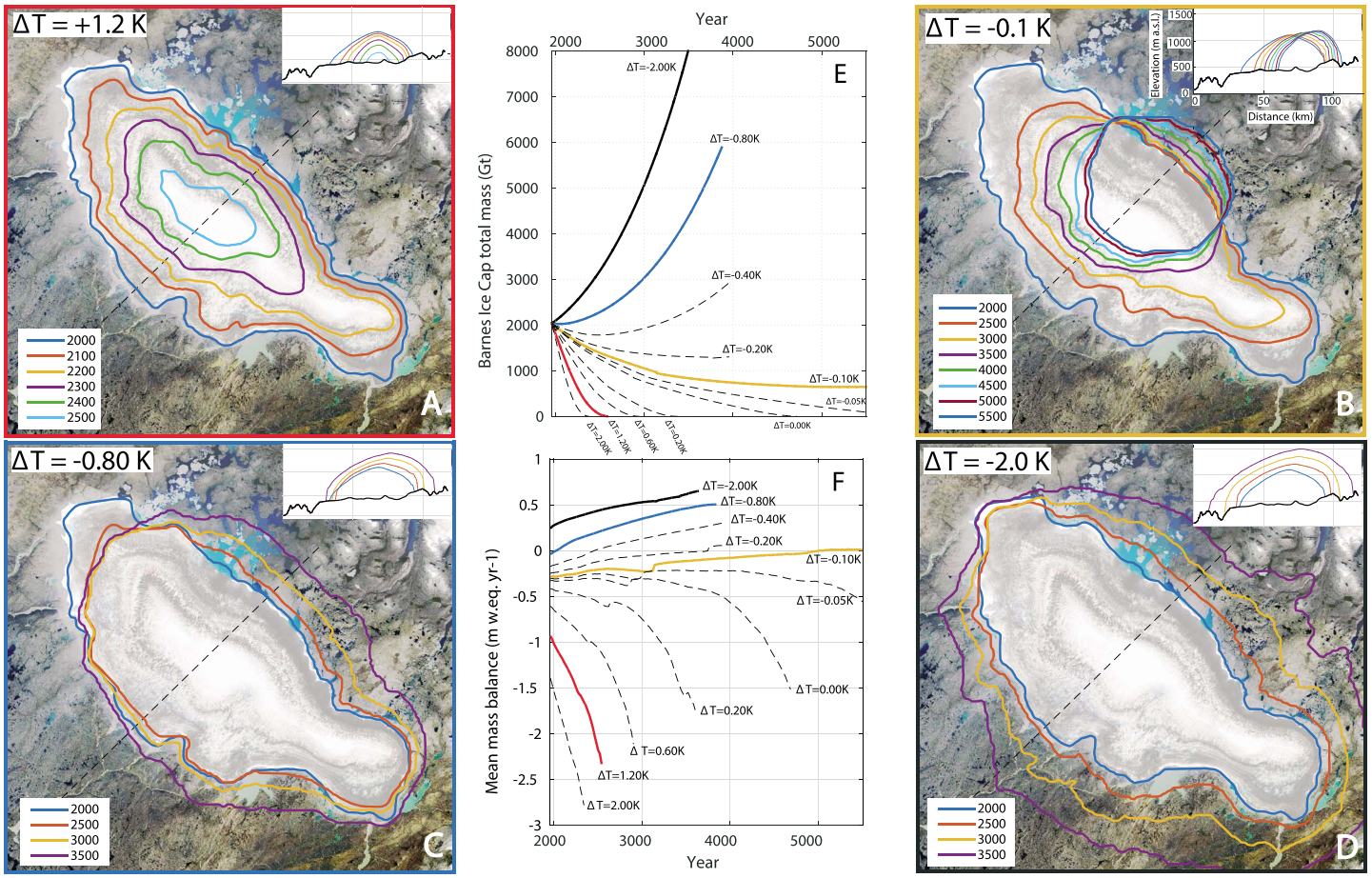

Figure 13. Modeled evolution of Barnes Ice Cap for different temperature forcings (a) $\Delta T = +1.2$ K. (b) $\Delta T = -0.1$ K. (c) $\Delta T = -0.8$ K. (d) $\Delta T = -2.0$ K. Model years are indicated in the bottom left of each panel. Insets show cross sections along the black dashed lines. (e) Evolution of total ice cap mass for various tests: red (Figure 13a), yellow (Figure 13b), blue (Figure 13c), and black (Figure 13d). (f) Evolution of mean surface mass balance for various tests: red (Figure 13a), yellow (Figure 13b), blue (Figure 13c), and black (Figure 13d). Kinks in some of the simulated trajectories arise from the separation of the south dome and the main ice cap.

resulting in an imbalance between surface mass balance and ice flux (Figure 14c). The net result is an upslope migration of the ice cap. Flat bedrock leads to a steady divide position (Figure 14a) and a symmetric ice cap geometry. The sloping bedrock under Barnes explains its tendency to advance to the northeast and the stability of the northeast margin relative to the southwest margin. The enhanced ice flux due to sliding along the southwest margin has modified the ice cap hypsometry and thus its mass balance on this side, further contributing to the preferential retreat of the southwest margin and related divide migration.

5.3.2. Sensitivity to Climate

To investigate the sensitivity of Barnes to climate, we perform 2000 year simulations (starting in 1960) for different precipitation and temperature anomalies. This period is long enough to observe the influence of the mass balance-elevation feedback. Due to the tendency of Barnes to adjust its form, as highlighted in the previous section, even a negative net balance applied to the current ice cap may lead to ice cap growth after several centuries (Figure 15). We define two quantities in order to characterize the ice cap response to climate: the linear mass balance trend (kg m^{-2} yr^{-2}) (linear fit to the mass balance evolution in time, Figure 15a) and the mean mass balance (kg m^{-2} yr^{-1}) for the initial shape in 1960 (Figure 15b). The sign of the mass balance trend determines whether the ice cap will survive. The climate threshold for ice cap survival is represented by the black line in Figure 15a and is denoted ΔT_{lim}. For example, if ΔT is 0.5 K and f_p is 1.1, the mean mass balance over the ice cap will be $\sim -5.0 \times 10^{-1}$ kg m^{-2} yr^{-1} (Figure 15b) and the trend will be $\sim$-1.0 $\times 10^{-3}$ kg m^{-2} yr^{-1} per year (Figure 15a); in this case the ice cap will disappear. However, if ΔT is -0.5 K and f_p is 1.1, the mean mass balance will be $\sim -1.0 \times 10^{-1}$ kg m^{-2} yr^{-1}, but the trend will be $\sim +2.0 \times 10^{-4}$ kg m^{-2} yr^{-1} per year; in this case the ice

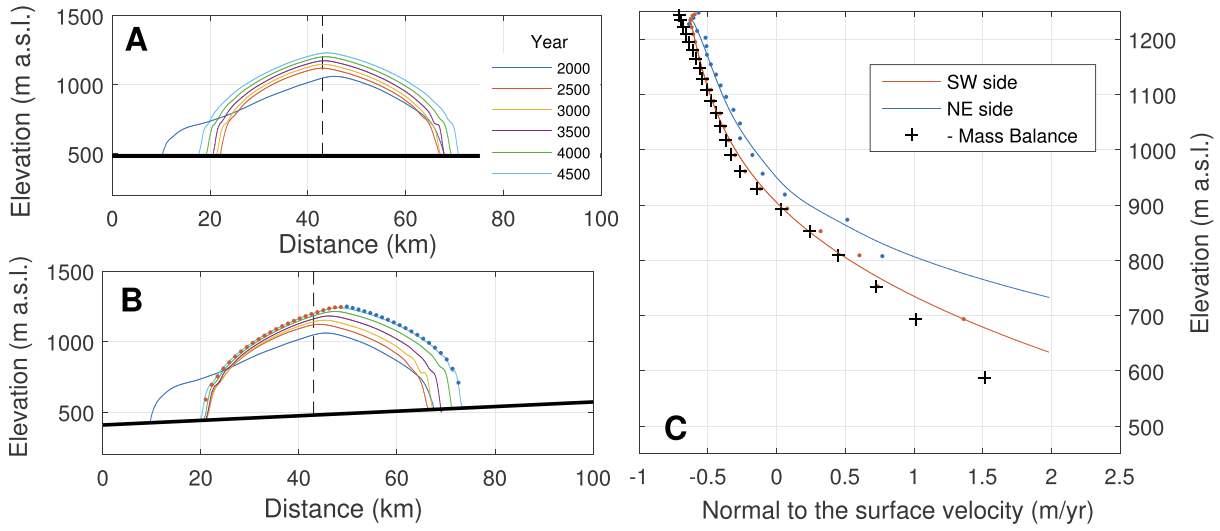

Figure 14. Cross section along the northeast-southwest axis of the ice cap: topographic evolution for a (a) flat and (b) inclined bed. Simulations assume no sliding and no PIL. (c) Surface-normal velocity for simulation in Figure 14b at 4500 CE and at locations of blue and red dots along profile. Associated fit is shown (blue and red lines) along with surface mass balance (black cross) as a function of elevation.

cap will survive. There is a climatic parameter space (hatched area, Figure 15b) in which Barnes will persist even though the current mass balance is negative, due to its dynamic adjustment and the mass balance-elevation feedback.

Figures 15c and 15d put this climate sensitivity into some perspective with a schematic Holocene climate as reconstructed for the Arctic and Baffin Island [from *Kaufman et al.*, 2004, 2009]. Although the climate sensitivity we compute is only valid for the current ice cap geometry, Figures 15c and 15d allow us to put our results in the context of the last 10,000 years. The results suggest strongly imbalanced conditions during the early Holocene (10 to 8 ka B.P.), in accordance with significant glacier and ice cap retreat around Barnes [*Briner et al.*, 2009], followed by a gradual evolution toward positive mass balance conditions in the Little Ice Age, commensurate with the relative stability of Barnes over recent millennia [*Briner et al.*, 2009]. Figure 15c shows that the last three millennia were characterized by a climate in which Barnes could sustain itself through dynamical adjustment. The latter part of the twentieth century marks the end of this period of stability and the beginning of a climate in which Barnes is unsustainable.

5.3.3. Influence of Surge Activity and Pleistocene Ice

The shape adjustment that determines the survival of the ice cap (section 5.3.2) could be affected by local dynamics related to surge activity and the influence of Pleistocene ice. Figure 16 shows the sensitivity of Barnes to sliding and the PIL. For example, a 0.05 K warming would result in a mass balance trend of $\sim -2.0\times10^{-4}\,\mathrm{kg\,m^{-2}\,yr^{-1}}$ per year if there were no residual Pleistocene ice at the bed; in this case Barnes would disappear. However, if one simply eliminated the sliding but retained the Pleistocene ice, the mass balance trend would be positive: $\sim +1.0\times10^{-4}\,\mathrm{kg\,m^{-2}\,yr^{-1}}$ per year. Figure 16 shows that if the 1960–2013 mean climate were maintained for 2000 years (within ±0.1 K), the fate of Barnes could be controlled by surge activity which tends to decrease the mean ice cap elevation and therefore its mean mass balance. It is interesting to note that the 1960–2013 mean climate ($\Delta T = 0$ K) has just crossed the threshold for Barnes' survival; the cessation of any sliding activity would be sufficient to preserve Barnes in this case. Figure 17 shows the evolution of Barnes for a constant present climate with $\Delta T = 0$ K, with and without sliding. In both cases the extremities of the long axis of the ice cap retreat rapidly, but after 1000 years the two simulations diverge: in the no sliding, no-Pleistocene-ice case, the ice cap begins to grow again, whereas under present conditions it continues to retreat and eventually disappears. The influence of the PIL is less than that of sliding since it affects ice cap stability in a narrow temperature range (hatched area in Figure 16) and for a limited amount of time as it is continuously thinning. The influence of the PIL is equivalent to less than a 0.08 K increase in air temperature and the influence of sliding to a 0.18 K increase and the combined influence of both to a 0.20 K increase.

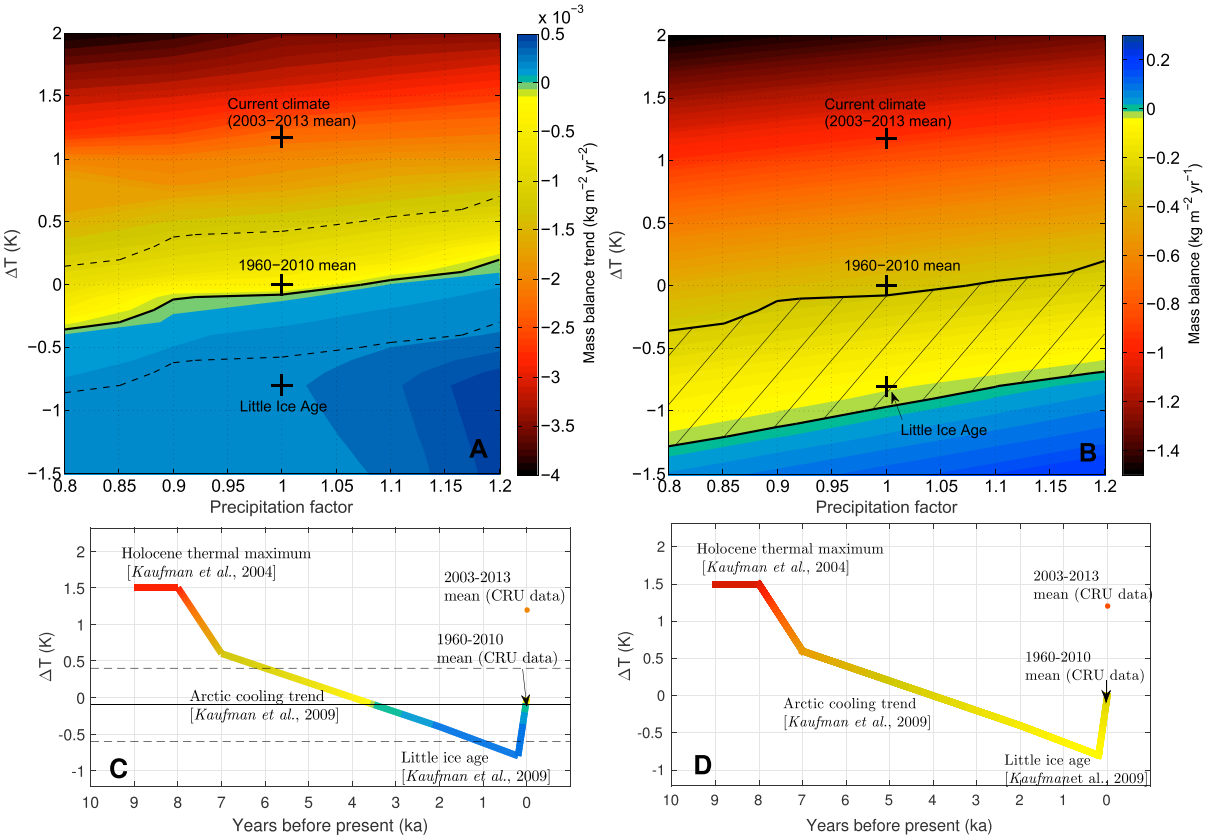

Figure 15. Sensitivity of Barnes Ice Cap to climate. (a) Surface mass balance trend over a 2000 year simulation as a function of precipitation and temperature anomalies (relative to the 1960–2013 reference). Blue area leads to ice cap growth and yellow/orange area leads to ice cap disappearance. Black line shows the threshold temperature anomaly for ice cap sustainability as function of precipitation with the associated uncertainty (black dashed lines) as estimated in section 6 (also present in Figure 15c). (b) Mean mass balance for the current ice cap geometry as a function of precipitation and temperature anomalies. Hatched zone represents the parameter space in which Barnes will survive despite its negative mass balance at present. (c and d) Schematic evolution of Holocene climate according to Kaufman *et al.* [2004, 2009]. Colors correspond to the quantities shown in Figures 15a and 15b, respectively.

6. Discussion of Model Uncertainty

Though uncertainties in the mass balance model are expected to be important, this study benefits from the number and diversity of available data that strongly constrain the mass balance model parameters (Table 1). The influence of dynamics on ice cap evolution is principally controlled by the initial 1960 ice cap shape, thickness, and basal conditions, which are respectively well constrained by the 1960 historical DEM, airborne radar measurements and the inversion of two independent sources of surface velocity data. However, the ice flow model that we have developed suffers some limitations that are difficult to overcome: (i) contrary to our assumptions, the 1960 thermal state of Barnes is not in equilibrium and is likely influenced by subglacial hydrology, past surges that are not captured by present measurements, and unsteady climate conditions of the past; (ii) prognostic simulations do not take into account any change in basal sliding conditions, and no sliding is assumed outside of the current ice cap margin; (iii) the PIL thickness distribution is poorly constrained; and (iv) lake calving is entirely neglected.

To investigate the sensitivity of our results to these shortcomings, additional simulations have been performed and model sensitivity quantified in terms of the change in threshold temperature anomaly for ice cap sustainability (ΔT_{lim}) (Table 2). These simple tests illustrate how the modeled stability of Barnes can be affected by parameter uncertainties and model limitations. Table 2 shows that degree-day factors for ice and snow affect the stability of Barnes differently, with the sensitivity to the degree-day factor for snow being 5 times greater than that for ice. This result arises from the fact that the degree-day factor for ice does not affect the accumulation zone and thus has minimal influence on the stability of Barnes, even though its shape can be affected. In contrast, the degree-day factor for snow directly affects the existence of the

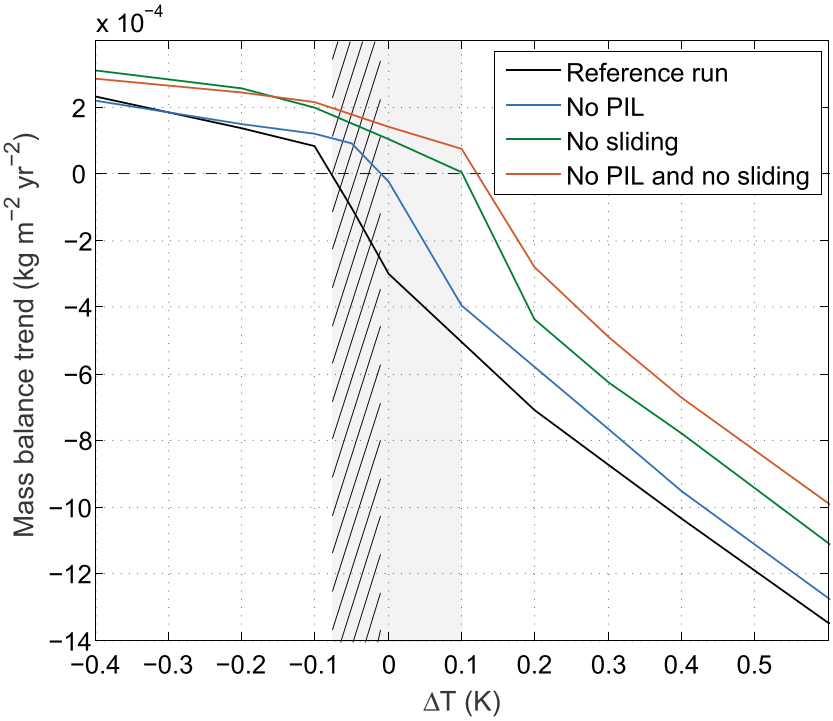

Figure 16. Surface mass balance trend during 2000 year simulations as a function of the temperature anomaly (relative to the 1960–2013 reference) for three different runs: a reference as in the section 5.3.2. (black line), one without the PIL (blue line), one without sliding (green line), and one without either the PIL or sliding (red line). Gray and hatched areas show the change in the threshold temperature anomaly for sustainability (ΔT_{lim}) for runs that neglect sliding and the PIL, respectively, relative to the reference run.

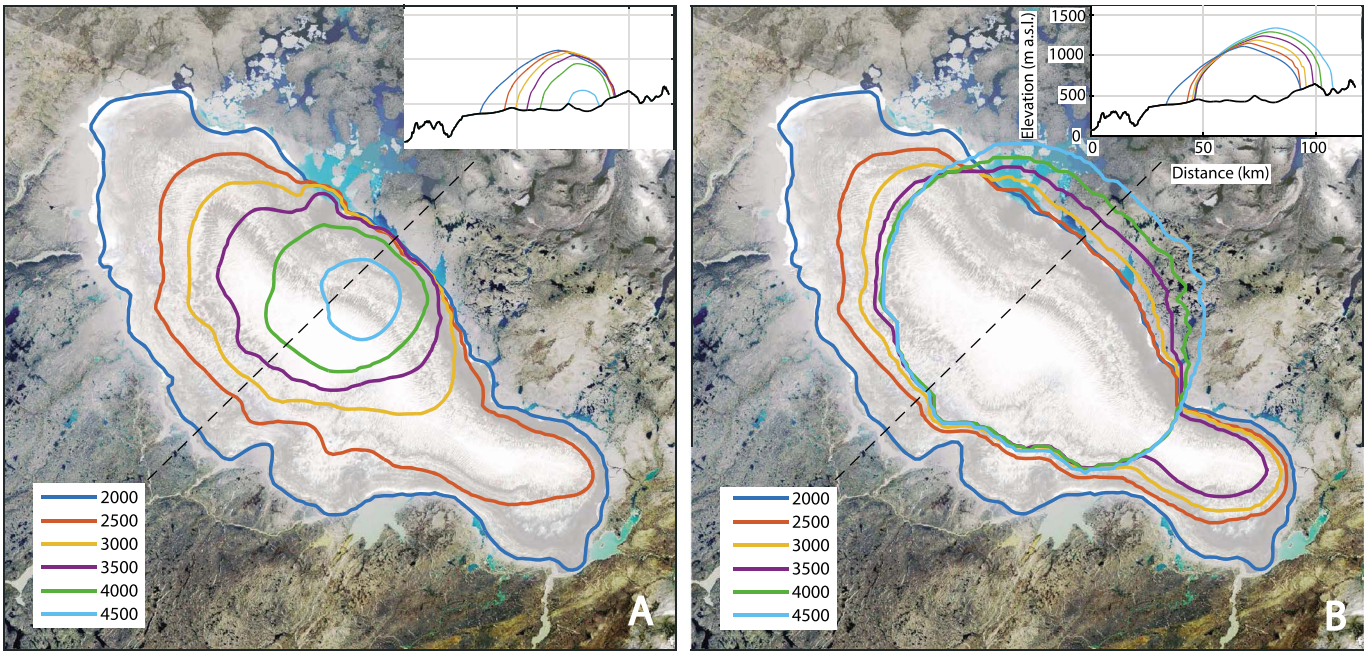

Figure 17. Modeled evolution of Barnes (a) with and (b) without sliding and PIL for the same climatic conditions ($\Delta T = 0$ K). Insets show cross sections along the dashed line. Legends in the bottom left of each panel indicate the year (CE) of the modeled ice cap edge.

Table 2. Modeled Threshold Temperature Anomaly for Sustainability (ΔT_{lim}) as Function of Different Model Parameter Values or Assumptions

Parameters (Units)	Reference Values or Sources	Tested Values	Modeled ΔT_{lim} (K)	Change in ΔT_{lim} (K)
Flow rate factor via the ice temperature (K)	Steady state computation	273.15/268.15/263.15	−0.4/−0.12/0.1	−0.3/−0.04/+0.2
β (MPa s m^{-1})	Inversion $\beta \in [10^{-3.5}\ 10^{-0.5}]$	$10^{-3}/10^{-2}$/no sliding	−1.3/−0.35/0.1	−1.2/−0.25/+0.2
β (outside current margin) (MPa s m^{-1})	No sliding	10^{-2}	−0.3	−0.2
Degree-day factor snow (kg m^{-2} K^{-1} d^{-1})	1.56×10^{-3}	$\pm 0.2 \times 10^{-3}$	−0.35/0.15	±0.25
Degree-day factor ice (kg m^{-2} K^{-1} d^{-1})	4.52×10^{-3}	$\pm 0.2 \times 10^{-3}$	−0.15/−0.05	±0.05

accumulation zone. Snow albedo should therefore be an important determinant of ice cap stability. Similar high sensitivities to degree-day factor for snow have been found on the Juneau Icefield (Alaska) by *Ziemen et al*. [2016]. Our estimated uncertainty in the degree-day factor for snow (see Table 1) introduces an uncertainty of 0.25 K in the threshold temperature anomaly for ice cap sustainability (ΔT_{lim}).

We estimate the influence of ice temperature by running the model with different constant and uniform ice temperatures (Table 2) that represent end-members: a temperate ice cap or a cold ice cap at 263.15 K. These extreme cases lead to a variation of −0.3 K and +0.2 K in ΔT_{lim}, respectively. The uncertainty arising from our modeled temperature field (limitation (i) above) thus has only moderate impact via the flow-law rate factor on ice cap stability, introducing an uncertainty that is probably less than 0.1 K in ΔT_{lim}. The sliding coefficient, by contrast, has a large impact on Barnes stability in the extreme case of high sliding everywhere. If β is set to the inferred value in the current fast flow zone ($\beta \sim 10^{-3}$ Mpa s m^{-1}), Barnes would be unstable even during the Little Ice Age. The sliding parameter is, however, initially well constrained by the inversion, and the uncertainty associated with the assumption of spatial and temporal invariance of β (limitation (ii)) would most likely be comparable in magnitude to the difference between low sliding everywhere ($\beta = 10^{-2}$ Mpa s m^{-1}) and no sliding (see Table 2). If we relax the assumption of no sliding outside of the current ice cap margin by fixing β outside the current margin to 10^{-2} MPa s m^{-1}, we find a decrease of 0.2 K in ΔT_{lim}.

Barnes' sensitivity to the PIL (limitation (iii)) has already been investigated in section 5.2.2. We find that ΔT_{lim} changes by less than 0.1 K as a function of PIL absence or presence (Figure 15a). The poor constraints on PIL thickness arise from the nonuniqueness inherent in the problem of disentangling basal sliding from enhanced deformation in the Pleistocene ice, using only surface velocities. Our methodology allows model uncertainty and data error to be compensated by adjustments to the basal sliding coefficient. In regions of low basal shear stress, PIL thickness can be highly sensitive to the inverted basal velocity (equation (16)), but as mentioned in section 5.2.2, the PIL affects ice flow only where basal shear stress is significant and thus in zones where the PIL thickness is well determined.

The influence of calving (limitation (iv)) is difficult to evaluate, and we have made no attempt to address this model shortcoming. Based on the current form and flow of the ice cap (see Figure 2), we might expect the presence of these lakes to contribute to enhanced but localized ice cap retreat.

Of the parameters tested, the stability of Barnes is most sensitive to the degree-day factor for snow. This parameter is, however, well constrained by the numerous surface mass balance data and introduces a limited uncertainty of 0.2 K on ΔT_{lim}. The uncertainty arising from the modeled dynamics would appear to be dominated by uncertainties in sliding, particularly its potential spatial and temporal evolution. Our tests yield less than 0.2 K of uncertainty on ΔT_{lim} as a function of sliding. The uncertainties linked to poorly modeled ice temperatures probably lead to changes in ΔT_{lim} less than 0.1 K. For a fixed precipitation amount, we estimate a total combined uncertainty on ΔT_{lim} of less than 0.5 K.

7. Conclusion

The retreat of the Laurentide Ice Sheet over Baffin Island [*Dyke and Prest*, 1987] has reached the state that we now know as Barnes Ice Cap. In this study, we combine historical in situ data sets with satellite observations to initialize a thermomechanical ice flow model to characterize the sensitivity of Barnes to climate and its internal dynamics. The model has been constrained using in situ surface mass balance and velocity measurements, airborne and satellite-based elevation change mapping, InSAR and ALOS-PALSAR velocity data sets, and borehole temperature and deformation measurements. Model innovations for this study include (i) a

method to estimate the influence of the low viscosity Pleistocene ice layer, (ii) combination of surface horizontal velocities, estimated elevation changes and modeled surface mass balance to invert for basal friction, and (iii) a new remeshing capability in Elmer/Ice to account for changes in ice cap geometry.

The mass balance modeling reveals no asymmetry across the northeast and southwest flanks of the ice cap in the elevation-mass balance relationship. The observed apparent asymmetry in mass balance [*Loken and Sagar*, 1967] is due to a lower mean elevation on the southwest flank; we do not find evidence of contrasting climatic conditions between the two sides. However, we confirm the existence of a positive accumulation gradient toward the southeast [*Loken and Sagar*, 1967], which explains why mean mass balance at the south dome summit is positive despite its elevation being lower than the north and central domes. We show that Barnes has lost 17% of its total mass between 1900 and 2010 and that the current (2000–2012) accumulation zone is now restricted to a small area of the central dome (Figure 5).

The dynamics of Barnes can be characterized by two different time scales: long-term dynamics driven by the adjustment of ice cap form originally imposed by the retreat of the Laurentide Ice Sheet and the topography of Baffin Island and short-term dynamics driven by sliding instabilities previously described as surges [*Holdsworth*, 1977]. The sliding zones are responsible for the formation of lobate structures along the southwest margin and are contributors to the ice cap asymmetry identified by *Mahaffy* [1976] using a Shallow Ice Approximation model. Among the five surge areas previously identified by *Holdsworth* [1977] (see Figure 1 in *Holdsworth* [1977] for areas numbers), our inversion for basal sliding velocities reveals one formerly active lobe (Area 4) and two currently active lobes (Areas 1 + 2 and 3). Our findings suggest, however, that Area 5 is most likely characterized by persistent sliding (rather than episodic surging) driven by temperate basal conditions that are sustained by frictional and deformational heat flux. In contrast, sliding under the south dome requires locally temperate basal conditions that cannot be sustained by energy supplied by the geothermal flux, ice deformation, and basal friction alone. Such sliding zones therefore require an additional energy supply, such as latent heat release from basal freeze-on.

The long-term dynamics of the ice cap are characterized by (i) higher rates of ice flow in the northeast-southwest direction and lower rates of ice flow in the northwest-southeast direction due to dynamical adjustment of the current ice cap form and (ii) higher upward surface-normal ice flux on the northeast flank due to the slope of the underlying bedrock. These tendencies allow for preferential retreat along the northwest and southeast margins, consistent with the reconstructions of ice cap retreat over the Holocene (Figure 1) [*Briner et al*., 2009; *Dyke and Prest*, 1987]. We also demonstrate that Barnes is influenced by enhanced ice deformation ($E \sim 3.1$) in the Pleistocene ice layer, particularly on long (millennial) time scales. Our sensitivity analysis shows that sliding instabilities are equivalent to a decrease of 0.2 K in the threshold temperature for ice cap sustainability. If the 1960–2013 mean climate persisted (in a range of ±0.2 K) over 2000 years, Barnes could disappear due to its sliding instabilities alone.

After emerging from a negative mass balance state during the early Holocene, Barnes entered a climate ~3 ka B.P. in which dynamical adjustment would permit ice cap survival. Barnes likely approached a state of slightly positive mass balance during the Little Ice Age, as evidenced by constructional moraines around much of its margin. The late twentieth century marked the return of an adverse climate for Barnes, with the 1960–2010 mean climate pushing the ice cap past its threshold of sustainability and toward its demise this millennium.

Acknowledgments

We are grateful for financial support provided by the Natural Sciences and Engineering Research Council of Canada and Simon Fraser University. This research was enabled in part by WestGrid (www.westgrid.ca) and Compute Canada/Calcul Canada (www.computecanada.ca). We thank Gerry Holdsworth for providing an abundance of original literature on Barnes, Roger Hooke and John Andrews for literature and conversations, Valentina Radić and Alex Cannon for supplying gridded climate data, and Dan Shugar for pointing us to the InSAR velocity data. We would like to thank 3vGeomatics Inc for the ERS SAR raw data sets and for providing access to their computer environment to calculate the InSAR displacement map. Bedrock topography data used in this paper were acquired by NASA's Operation IceBridge Project. Meteorological data are available on http://climate.weather.gc.ca/ and all other data used are available in the cited references or included in the figures of the manuscript. We are grateful to Roger Hooke and Andy Aschwanden for their careful reviews of the manuscript and to Bryn Hubbard for editorial oversight.

References

Abdalati, W., W. Krabill, E. Frederick, S. Manizade, C. Martin, J. Sonntag, R. Swift, R. Thomas, J. Yungel, and R. Koerner (2004), Elevation changes of ice caps in the Canadian Arctic Archipelago, *J. Geophys. Res.*, *109*, F04007, doi:10.1029/2003JF000045.

Andrews, J. T. (2002), Glaciers of Baffin Island, in *Glaciers of Canada*, *U.S. Geol. Prof. Pap. 1386-J-1*, edited by R. S. Williams and J. G. Ferrigno, pp. 165–195, U.S. Govt. Print. Off., Washington.

Andrews, J. T., and M. D. Barnett (1979), Holocene (Neoglacial) moraine and proglacial lake chronology, Barnes Ice Cap, Canada, *Boreas*, *8*, 341–358, doi:10.1111/j.1502-3885.1979.tb00817.x.

Andrews, J. T., and J. D. Ives (1978), "Cockburn" nomenclature and the late Quaternary history of the eastern Canadian Arctic, *Arct. Alp. Res.*, *10*(3), 617–633, doi:10.2307/1550683.

Aschwanden, A., E. Bueler, C. Khroulev, and H. Blatter (2012), An enthalpy formulation for glaciers and ice sheets, *J. Glaciol.*, *58*(209), 441–457, doi:10.3189/2012JoG11J088.

Bingham, R. G., P. W. Nienow, M. J. Sharp, and L. Copland (2006), Hydrology and dynamics of a polythermal (mostly cold) high Arctic glacier, *Earth Surf. Processes Landforms*, *31*(12), 1463–1479, doi:10.1002/esp.1374.

Blatter, H. (1987), On the thermal regime of an Arctic valley glacier: A study of White Glacier, Axel Heiberg Island, NWT, Canada, *J. Glaciol.*, *33*(114), 200–211.
Blatter, H., and K. Hutter (1991), Polythermal conditions in Arctic glaciers, *J. Glaciol.*, *37*(126), 261–269.
Braithwaite, R. J. (1995), Positive degree-day factors for ablation on the Greenland ice sheet studied by energy-balance modelling, *J. Glaciol.*, *41*(137), 153–160.
Briner, J. P., P. T. Davis, and G. H. Miller (2009), Latest Pleistocene and Holocene glaciation of Baffin Island, Arctic Canada: Key patterns and chronologies, *Quat. Sci. Rev.*, *28*(21), 2075–2087, doi:10.1016/j.quascirev.2008.09.017.
Clarke, G. K., S. G. Collins, and D. E. Thompson (1984), Flow, thermal structure, and subglacial conditions of a surge-type glacier, *Can. J. Earth Sci.*, *21*(2), 232–240, doi:10.1139/e84-024.
Classen, D. F. (1977), Temperature profiles for the Barnes Ice Cap surge zone, *J. Glaciol.*, *18*(80), 391–405.
Copland, L., and M. Sharp (2001), Mapping thermal and hydrological conditions beneath a polythermal glacier with radio-echo sounding, *J. Glaciol.*, *47*(157), 232–242.
Copland, L., M. J. Sharp, and J. A. Dowdeswell (2003), The distribution and flow characteristics of surge-type glaciers in the Canadian High Arctic, *Ann. Glaciol.*, *36*(1), 73–81, doi:10.3189/172756403781816301.
Cuffey, K., and W. B. S. Paterson (2010), *The Physics of Glaciers*, 4th ed., Academic, Amsterdam.
Dowdeswell, E. K., J. A. Dowdeswell, and F. Cawkwell (2007), On the glaciers of Bylot Island, Nunavut, Arctic Canada, *Arct. Antarct. Alp. Res.*, *39*(3), 402–411, doi:10.1657/1523-0430(05-123)[DOWDESWELL]2.0.CO;2.
Dupont, F. (2013), Télédétection micro-onde de surfaces enneigées en milieu arctique: Étude des processus de surface de la calotte glaciaire Barnes, Nunavut, Canada, PhD thesis, Univ. of Grenoble, France.
Dupont, F., A. Royer, A. Langlois, A. Gressent, G. Picard, M. Fily, P. Cliche, and M. Chum (2012), Monitoring the melt season length of the Barnes Ice Cap over the 1979–2010 period using active and passive microwave remote sensing data, *Hydrol. Processes*, *26*(17), 2643–2652, doi:10.1002/hyp.9382.
Dyke, A. S., and Prest, V. K. (1987), Late Wisconsinan and Holocene retreat of the Laurentide ice sheet, Geol. Surv. of Canada, "A" Series Map 1702A, doi:10.4095/122842.
Dyke, A. S., A. Moore and L. Robertson (2003), Deglaciation of North America, *Geol. Surv. Open File Rep. 1574*, Ottawa.
Gagliardini, O., et al. (2013), Capabilities and performance of Elmer/Ice, a new-generation ice sheet model, *Geosci. Model Dev.*, *6*, 1299–1318, doi:10.5194/gmd-6-1299-2013.
Gardner, A., G. Moholdt, A. Arendt, and B. Wouters (2012), Accelerated contributions of Canada's Baffin and Bylot Island glaciers to sea level rise over the past half century, *The Cryosphere*, *6*, 1103–1125, doi:10.5194/tc-6-1103-2012.
Gardner, A. S., M. J. Sharp, R. M. Koerner, C. Labine, S. Boon, S. J. Marshall, D. O. Burgess, and D. Lewis (2009), Near-surface temperature lapse rates over arctic glaciers and their implications for temperature downscaling, *J. Clim.*, *22*(16), 4281–4298, doi:10.1175/2009JCLI2845.1.
Gardner, A. S., G. Moholdt, B. Wouters, G. J. Wolken, D. O. Burgess, M. J. Sharp, J. C. Cogley, C. Braun, and C. Labine (2011), Sharply increased mass loss from glaciers and ice caps in the Canadian Arctic Archipelago, *Nature*, *473*(7347), 357–360, doi:10.1038/nature10089.
Gilbert, A., C. Vincent, P. Wagnon, E. Thibert, and A. Rabatel (2012), The influence of snow cover thickness on the thermal regime of Tête Rousse Glacier (Mont Blanc range, 3200 m asl): Consequences for outburst flood hazards and glacier response to climate change, *J. Geophys. Res.*, *117*, F04018, doi:10.1029/2011JF002258.
Gilbert, A., O. Gagliardini, C. Vincent, and P. Wagnon (2014), A 3-D thermal regime model suitable for cold accumulation zones of polythermal mountain glaciers, *J. Geophys. Res. Earth Surf.*, *119*, 1876–1893, doi:10.1002/2014JF003199.
Gillet-Chaulet, F., O. Gagliardini, H. Seddik, M. Nodet, G. Durand, C. Ritz, T. Zwinger, R. Greve, and D. G. Vaughan (2012), Greenland ice sheet contribution to sea-level rise from a new-generation ice-sheet model, *The Cryosphere*, *6*, 1561–1576, doi:10.5194/tc-6-1561-2012.
Gray, L., D. Burgess, L. Copland, M. N. Demuth, T. Dunse, K. Langley, and T. V. Schuler (2015), CryoSat-2 delivers monthly and inter-annual surface elevation change for Arctic ice caps, *The Cryosphere*, *9*(5), 1895–1913, doi:10.5194/tc-9-1895-2015.
Hock, R. (2003), Temperature index melt modelling in mountain areas, *J. Hydrol.*, *282*, 104–115, doi:10.1016/S0022-1694(03)00257-9.
Holdsworth, G. (1977), Surge activity on the Barnes Ice Cap, *Nature*, *269*, 588–590, doi:10.1038/269588a0.
Holdsworth, G., and R. L. Hooke (1977), *Fluctuations of the Uncertainty in the Horizontal Position of the Stakes Arises Glaciers 1970-74*, vol. III, edited by Müller, Assoc. of Hydrol. Sci. - United Nations Educational, Sci. and Cultural Organization.
Hooke, R. L. (1976), Pleistocene ice and the base of the Barnes Ice Cap, Canada, *J. Glaciol.*, *17*(75), 49–60.
Hooke, R. L., and H. B. Clausen (1982), Wisconsin and holocene δ18O variations, Barnes Ice Cap, Canada, *Geol. Soc. Am. Bull.*, *93*(8), 784–789.
Hooke, R. L., and B. Hanson (1986), Borehole deformation experiment, Barnes Ice Cap, Canada, *Cold Reg. Sci. Technol.*, *12*, 261–276, doi:10.1016/0165-232X(86)90039-X.
Hooke, R. L., E. C. Alexander, and R. J. Gustafson (1980), Temperature profiles in the Barnes Ice Cap, Baffin Island, Canada, and heat flux from the subglacial terrane, *Can. J. Earth Sci.*, *17*, 1174–1188, doi:10.1139/e80-124.
Hooke, R. L. B., J. E. Gould, and J. Brzozowski (1983), Near-surface temperatures near and below the equilibrium line on polar and subpolar glaciers, *Z. Gletscherk. Glazialgeol.*, *19*(1), 1–25.
Hooke, R. L., G. W. Johnson, K. A. Brugger, B. Hanson, and G. Holdsworth (1987), Changes in mass balance, velocity, and surface profile along a flow line on Barnes Ice Cap, 1970–1984, *Can. J. Earth Sci.*, *24*, 1550–1561, doi:10.1139/e87-151.
Hutchinson, M. F., D. W. McKenney, K. Lawrence, J. H. Pedlar, R. F. Hopkinson, E. Milewska, and P. Papadopol (2009), Development and testing of Canada-wide interpolated spatial models of daily minimum–maximum temperature and precipitation for 1961–2003, *J. Appl. Meteorol. Climatol.*, *48*, 725–741, doi:10.1175/2008JAMC1979.1.
Jacobs, J. D., R. Heron, and J. E. Luther (1993), Recent changes at the northwest margin of the Barnes Ice Cap, Baffin Island, NWT, Canada, *Arct. Alp. Res.*, *25*(4), 341–352, doi:10.2307/1551917.
Jacobs, J. D., É. L. Simms, and A. Simms (1997), Recession of the southern part of Barnes Ice Cap, Baffin Island, Canada, between 1961 and 1993, determined from digital mapping of Landsat TM, *J. Glaciol.*, *43*(143), 98–102.
Jones, P. D., D. H. Lister, T. J. Osborn, C. Harpham, M. Salmon, and C. P. Morice (2012), Hemispheric and large-scale land-surface air temperature variations: An extensive revision and an update to 2010, *J. Geophys. Res.*, *117*, D05127, doi:10.1029/2011JD017139.
Kaufman, D., et al. (2009), Recent warming reverses long-term Arctic cooling, *Science*, *325*, 1236–1239, doi:10.1126/science.1173983.
Kaufman, D. S., et al. (2004), Holocene thermal maximum in the western Arctic (0–180 W), *Quat. Sci. Rev.*, *23*(5), 529–560, doi:10.1016/j.quascirev.2003.09.007.
Lenaerts, J. T. M., J. H. van Angelen, M. R. van den Broeke, A. S. Gardner, B. Wouters, and E. van Meijgaard (2013), Irreversible mass loss of Canadian Arctic Archipelago glaciers, *Geophys. Res. Lett.*, *40*, 870–874, doi:10.1002/grl.50214.

Loken O. H., and R. B. Sagar (1967), Mass balance observation on the Barnes Ice Cap, Baffin Island, Canada, Commission of Snow and Ice, General Assembly of Bern, Sept-Oct, 282-290.

Loken O. H., A. Geiger and P. Langlais (1968), North-Central Baffin Island field report, 1967. Surface movement and strain net measurements-Barnes Ice Cap, Can. Dep. Energy, Mines and Resources, Inland Waters Br., Rep. Ser. No. 2, 97-102.

MacAyeal, D. R. (1992), The basal stress distribution of Ice Stream E, Antarctica, inferred by control methods, *J. Geophys. Res.*, *97*, 595–603, doi:10.1029/91JB02454.

Mahaffy, M. W. (1976), A three dimensional numerical model of ice sheets: Tests on the Barnes Ice Cap, Northwest Territories, *J. Geophys. Res.*, *81*, 1059–1066, doi:10.1029/JC081i006p01059.

Mekis, E., and W. D. Hogg (1999), Rehabilitation and analysis of Canadian daily precipitation time series, *Atmos. Ocean*, *37*, 53–85, doi:10.1080/07055900.1999.9649621.

Murray, T., T. Strozzi, A. Luckman, H. Jiskoot, and P. Christakos (2003), Is there a single surge mechanism? Contrasts in dynamics between glacier surges in Svalbard and other regions, *J. Geophys. Res.*, *108*(B5), 2237, doi:10.1029/2002JB001906.

Radić, V., and R. Hock (2010), Regional and global volumes of glaciers derived from statistical upscaling of glacier inventory data, *J. Geophys. Res.*, *115*, F01010, doi:10.1029/2009JF001373.

Reeh, N. (1985), Was the Greenland ice sheet thinner in the late Wisconsinan than now?, *Nature*, *317*(6040), 797–799, doi:10.1038/317797a0.

Sagar, R. B. (1966), Glaciological and climatological studies on the Barnes Ice Cap, 1962-64, *Geogr. Bull.*, *8*, 3–47.

Senese, A., M. Maugeri, E. Vuillermoz, C. Smiraglia, and G. Diolaiuti (2014), Using daily air temperature thresholds to evaluate snow melting occurrence and amount on Alpine glaciers by T-index models: The case study of the Forni Glacier (Italy), *The Cryosphere*, *8*(5), 1921–1933, doi:10.5194/tc-8-1921-2014.

Sharp, M., D. O. Burgess, J. G. Cogley, M. Ecclestone, C. Labine, and G. J. Wolken (2011), Extreme melt on Canada's Arctic ice caps in the 21st century, *Geophys. Res. Lett.*, *38*, L11501, doi:10.1029/2011GL047381.

Sneed, W. A., R. L. Hooke, and G. S. Hamilton (2008), Thinning of the south dome of Barnes Ice Cap, Arctic Canada, over the past two decades, *Geology*, *36*(1), 71–74, doi:10.1130/G24013A.1.

Van Wychen, W., L. Copland, D. O. Burgess, L. Gray, and N. Schaffer (2015), Glacier velocities and dynamic discharge from the ice masses of Baffin and Bylot Islands, Nunavut, Canada, *Can. J. Earth Sci.*, doi:10.1139/cjes-2015-0087.

Ziemen, F. A., R. Hock, A. Aschwanden, C. Khroulev, C. Kienholz, A. Melkonian, and J. Zhang (2016), Modeling the evolution of the Juneau Icefield between 1971 and 2100 using the Parallel Ice Sheet Model (PISM), *J. Glaciol.*, *62*(231), 199–214, doi:10.1017/jog.2016.13.